Monthly Notices of the ROYAL ASTRONOMICAL SOCIETY

MNRAS **537,** 580–597 (2025) https://doi.org/10.1093/mnras/staf012
Advance Access publication 2025 January 6

An analytic model of gravitational collapse induced by radiative cooling: instability scale, density profile, and mass infall rate

James Gurian [1], Boyuan Liu [2,3]★ Donghui Jeong [4,5] Takashi Hosokawa [6], Shingo Hirano [7,8] and Naoki Yoshida [9,10,11]

[1]*Perimeter Institute for Theoretical Physics, Waterloo, ON N2L 2Y5, Canada*
[2]*Institute of Astronomy, University of Cambridge, Madingley Road, Cambridge CB3 0HA, UK*
[3]*Institut für Theoretische Astrophysik, Zentrum für Astronomie, Universität Heidelberg, Albert Ueberle Straße 2, D-69120 Heidelberg, Germany*
[4]*Department of Astronomy and Astrophysics and Institute for Gravitation and the Cosmos, The Pennsylvania State University, University Park, PA 16802, USA*
[5]*School of Physics, Korea Institute for Advanced Study (KIAS), 85 Hoegiro, Dongdaemun-gu, Seoul 02455, Republic of Korea*
[6]*Department of Physics, Kyoto University, Sakyo, Kyoto 606-8502, Japan*
[7]*Department of Astronomy, School of Science, University of Tokyo, 7-3-1 Hongo, Bunkyo, Tokyo 113-0033, Japan*
[8]*Department of Applied Physics, Faculty of Engineering, Kanagawa University, Kanagawa 221-0802, Japan*
[9]*Department of Physics, School of Science, The University of Tokyo, 7-3-1 Hongo, Bunkyo, Tokyo 113-0033, Japan*
[10]*Research Center for the Early Universe, School of Science, The University of Tokyo, 7-3-1 Hongo, Bunkyo, Tokyo 113-0033, Japan*
[11]*Kavli Institute for the Physics and Mathematics of the Universe (WPI), The University of Tokyo, Kashiwa, Chiba 277-8583, Japan*

Accepted 2024 December 24. Received 2024 November 28; in original form 2024 August 23

ABSTRACT

We present an analytic description of the spherically symmetric gravitational collapse of radiatively cooling gas clouds, which illustrates the mechanism by which radiative cooling induces gravitational instability at a characteristic mass scale determined by the microphysics of the gas. The approach is based on developing the density–temperature relationship of the gas into a full dynamical model. We convert the density–temperature relationship into a barotropic equation of state, based on which we develop a refined instability criterion and calculate the density and velocity profiles of the gas. From these quantities, we determine the time-dependent mass infall rate on to the centre of the cloud. This approach distinguishes the rapid, quasi-equilibrium contraction of a cooling gas core to high central densities from the legitimate instability this contraction establishes in the envelope. We explicate the model in the context of a primordial mini-halo cooled by molecular hydrogen, and then provide two further examples: a delayed collapse with hydrogen deuteride cooling and the collapse of an atomic-cooling halo. In all three cases, we show that our results agree well with full hydrodynamical treatments.

Key words: hydrodynamics – stars: Population III – dark ages, reionization, first stars.

1 INTRODUCTION

Gravitational collapse leads to the formation of objects (e.g. stars, degenerate stars, black holes, and planets) with densities tens of orders of magnitude above the cosmic mean. The physics relevant to the collapse include, at the bare minimum, gravitation, thermal pressure, and radiative cooling. Historically, these dynamics could be modelled only under very restrictive assumptions amenable to analytic or – by modern standards – quite primitive numerical techniques. Today, the relevant physical processes can be included in great detail in sophisticated numerical simulations. Such studies have yielded powerful insights into the physics of gravitational collapse and star formation in a wide range of environments. However, the very complexity of these simulations can obscure the physical interpretation of the results. Moreover, there is increasing interest both in dark matter models which modify the gas collapse and star formation processes (e.g. due to exotic energy injection, Ripamonti, Mapelli & Ferrara 2007; Freese et al. 2016; Qin et al. 2024) and in the possibility that dark matter could itself cool and collapse to form dark compact objects (D'Amico et al. 2018; Shandera, Jeong & Grasshorn Gebhardt 2018; Chang et al. 2019; Gurian et al. 2022; Hippert et al. 2022; Bramante et al. 2024a; Bramante, Diamond & Kim 2024b). In the face of large model and parameter spaces, state-of-the-art numerical treatments become rapidly intractable. It is thus a desirable goal to synthesize and distill the lessons learned from state-of-the art simulations into expository theories which (thanks to enormous advances in computational power) no longer need be restricted to such extremely idealized situations. A particularly appealing theoretical target is the characteristic mass of gravitationally unstable clouds in which these objects form. While the mass function of the eventual collapsed objects depends on various complex physical processes, the typical mass of the natal collapsing clouds imposes an overall scale on the problem.

Analytic descriptions and heuristics describing the collapse of gases governed by simple equations of state (i.e. isothermal or polytropic) are well established in the literature (e.g. Larson 1969; Penston 1969; Hunter 1977; Shu 1977). We mention in particular two

★ E-mail: treibeis1995@gmail.com

© 2025 The Author(s).
Published by Oxford University Press on behalf of Royal Astronomical Society. This is an Open Access article distributed under the terms of the Creative Commons Attribution License (https://creativecommons.org/licenses/by/4.0/), which permits unrestricted reuse, distribution, and reproduction in any medium, provided the original work is properly cited.

Downloaded from https://academic.oup.com/mnras/article/537/1/580/7943696 by guest on 09 March 2025

similarity solutions: the first derived by Larson (1969) and Penston (1969) (hereafter referred to as the Larson–Penston solution) and the second by Shu (1977) (the Shu solution). The former describes the highly dynamical collapse of a Bonnor–Ebert sphere, while the latter describes the quasi-static collapse of a singular isothermal sphere triggered by the propagation of a rarefaction wave after core formation. Simulations typically reveal an intermediate picture, where the gas is accelerated towards the Larson–Penston solution over the course of the collapse (Foster & Chevalier 1993; McKee & Tan 2002, 2003; Tan & McKee 2004; Omukai, Hosokawa & Yoshida 2010).

While similarity solutions are exact under the appropriate assumptions, they are by definition scale-free. That is to say they provide no information about the beginning, end, or mass scale of the collapse. The canonical scale associated with the onset of gravitational collapse is the Jeans scale, which describes a balance between pressure gradients and gravity (Jeans 1928), given as

$$M_{\rm J} \approx 1.44 \left(\frac{k_{\rm B} \bar{T}}{\mu m_{\rm P} G} \right)^{3/2} \bar{\rho}^{-1/2}, \tag{1}$$

where $k_{\rm B}$ is the Boltzmann constant, $\bar{T}$ is the average temperature, $\bar{\rho}$ is the average density, μ is the mean molecular weight, and G is the gravitational constant. The intuition is that at small scales pressure damps out perturbations while at large scales gravity overwhelms pressure support. This argument was later refined by Ebert (1955) and Bonnor (1956) as the Bonnor–Ebert mass, discussed in detail below. Calculating the Jeans mass requires a fixed density and temperature. To use the Jeans mass to pick out a scale for the onset of gravitational collapse is justified when the spatial density structure of the gas is independent of its pressure, for example, if the density probability distribution is set by the statistics of turbulence (i.e. Hopkins 2012a, 2013).

In fact, as the density in a gas cloud increases the Jeans mass will decreases as long as T increases more slowly than ρ^3. A consequence is that over the course of the collapse, progressively smaller scales can become unstable. This process of 'hierarchical fragmentation' is ultimately terminated when the gas becomes optically thick and unable to cool efficiently. For stars, the opacity limit is of the order of $10^{-3}\,{\rm M}_\odot$ (Rees 1976). Still, the opacity-limited Jeans mass has often been adopted in the dissipative dark matter literature as a heuristic for the final mass of the hydrostatic objects produced by the collapse, either directly (Chang et al. 2019; Bramante et al. 2024a, b; Fernandez et al. 2024) as a lower bound (Gurian et al. 2022), or with a constant multiplicative enhancement (Shandera et al. 2018).

An alternative argument picks out a preferred scale in the collapse based on deviations from isothermality, which alter the effective equation of state of the gas. It is widely appreciated that when the temperature is an increasing function of density fragmentation is suppressed, while when temperature is a decreasing function of density fragmentation is enhanced (Larson 1985, 2005; Li, Klessen & Mac Low 2003). These observations are theoretically best justified in the case of filamentary geometries (Ostriker 1964; Inutsuka & Miyama 1992; Omukai et al. 2005). On the other hand, fragmentation in the sense of growth of initially small perturbations at some preferred scale has been shown to be ineffective during global free-fall collapse (Bodenheimer, Tohline & Black 1980; Tohline 1980a, b).

Neither Jeans-based argument explicitly considers the (in)efficiency of radiative cooling. Without cooling, a Jeans unstable cloud compressionally heats to a new equilibrium. On the other hand, in the presence of efficient radiative cooling even a Jeans stable cloud will contract on its cooling time-scale, which may be comparable to its free-fall time-scale (Bromm, Coppi & Larson 1999; Gurian, Jeong & Liu 2024). Radiative cooling is explicitly accounted for in the Rees–Ostriker criterion (Rees & Ostriker 1977). The argument is that a gas which can cool within its dynamical (free-fall) time-scale will undergo dynamical collapse and fragmentation. This calculation requires single, characteristic values for the temperature and density. In general, the gas will have some density, temperature, and chemical composition gradients. The cooling and free-fall time-scales can be quite sensitive, non-linear functions of these quantities. It is not obvious that a naive average of these quantities over some region will produce a physically reasonable mass scale for the onset of the collapse. Bertschinger (1989) and White & Frenk (1991) accounted for this fact by calculating the 'cooling radius', defined as the radius at which the local cooling time (in some assumed density profile) equals the age of the system. In particular, Bertschinger (1989) discovered a similarity solution based on this length scale for the evolution of the cooling gas. However, the similarity exists only for power-law (i.e. scale-free) density and pressure profiles. Cooling can modify the effective equation of state of the gas in a scale-dependent manner, which limits the applicability of the solution. Moreover, the scale at which cooling becomes efficient does not necessarily correspond to the onset of gravitational instability or fragmentation. An efficiently cooling core of a gas cloud can remain quasi-hydrostatic in structure if the sound crossing time is sufficiently short, while fragmentation depends on small-scale density perturbations.

As detailed above, this extensive prior work does not fully succeed in defining the characteristic mass scale of gravitational instability in all contexts. The shortcomings of these heuristics are clearly illustrated in the context of the formation of first generation, Pop. III stars. In pristine (metal-free) gas, the only significant coolants are molecular hydrogen (H_2), hydrogen deuteride (HD), and atomic hydrogen (H) (Liu & Bromm 2018). In the canonical case of mini-haloes cooled by molecular hydrogen, gravitational instability has long been associated with the Jeans scale at the minimum temperature over the course of the collapse, i.e. the 'loitering point' (Bromm et al. 1999), $\sim 10^3\,{\rm M}_\odot$. This minimum temperature occurs at the critical density of molecular hydrogen, where collisional de-excitation begins to compete with radiative de-excitation. However, radiative cooling typically becomes efficient (in the sense that the cooling time-scale becomes as short as the dynamical time-scale) at a lower density and larger mass scale 10^4–$10^5\,{\rm M}_\odot$. Moreover, the early phase of the collapse is monolithic, with typically only one star-forming cloud per halo. That is, fragmentation into multiple Jeans-scale clumps does not actually occur and should not be invoked as an explanation for this characteristic mass.

Here, we show that the characteristic scale of this gravitational instability can be explained by the non-homologous nature of the collapse, as a rapidly cooling (Rees–Ostriker unstable) but perturbatively (Jeans/Bonnor–Ebert) stable core of gas contracts and establishes an out-of-equilibrium density profile in its envelope. The degree of instability in this envelope determines the subsequent infall rate on to the protostar and its disc. To this end, we develop a dynamical model of gravitational collapse which explicitly includes thermal pressure, gravity, and radiative cooling. As our test-bed, we consider the collapse of primordial gas into first generation (Pop. III) stars, where the initial conditions for the collapse are dictated by the cosmological environment, and can be described in terms of a relatively small number of physical quantities. Still, a wide range of outcomes are possible for the collapse, and the resulting Pop. III initial mass function remains a topic of active research (for reviews see Bromm & Larson 2004; Bromm 2013; Haemmerlé et al. 2020;

Downloaded from https://academic.oup.com/mnras/article/537/1/580/7943696 by guest on 09 March 2025

Klessen & Glover 2023). As discussed above, the radiative cooling physics are thought to play a crucial role in setting the mass-scale of the gravitational collapse. In addition to molecular hydrogen, the formation of deuterated hydrogen (which has a permanent dipole moment) leads to a lower minimum temperature and less massive collapsing cloud (Ripamonti et al. 2007; Hirano et al. 2014; Nishijima, Hirano & Umeda 2024), while nearly isothermal atomic cooling is associated with direct collapse and the formation of supermassive stars (Omukai et al. 2005; Latif et al. 2013; Wise et al. 2019; Kiyuna, Hosokawa & Chon 2023).

In all these cases, cooling remains efficient until the formation of a protostar. For this reason, the density in the centre of the cloud rapidly increases *independent* of the gravitational stability of the cloud. As the density increases, the core becomes both smaller and less massive. If cooling remains efficient indefinitely, the endpoint of the contraction phase is an infinitely concentrated and infinitesimally small core. It is this core-contraction which can (but does not necessarily) establish true gravitational instability in the surrounding envelope. We demonstrate here that the mass scale of this gravitational instability in the envelope is controlled by features in the temperature–density relationship.

Our model uses the density and temperature-dependent radiative cooling rates to determine the quantity of gravitationally unstable gas 'left behind' by the core-contraction, and to estimate the rate at which this gas will fall on to the protostar, or its accretion disc. The model is based on defining an effective barotropic equation of state for the gas from the thermal evolution in the core, which in this work we supply using a one-zone model. We demonstrate the importance of a modified Bonnor–Ebert (MBE) scale in regulating the contraction of the core. We use this scale to calculate a radial density profile for the gas, including both the pressure-supported core and the envelope established by the core contraction. We assess the gravitational (in)stability of the envelope by the ratio of the mass enclosed to the MBE mass, $\kappa_{\rm MBE}$. Finally, we determine the time-dependent mass infall rate from the envelope on to the central hydrostatic core, which we connect to $\kappa_{\rm MBE}$. The model preserves the physical transparency and computational expediency of analytic approaches while including the full temperature and density dependence of the relevant cooling rates.

The calculation is perhaps most similar in spirit to the series of papers Sipilä, Harju & Juvela (2011, 2015) and Sipilä, Caselli & Juvela (2017), which calculated a Bonnor–Ebert stability criterion for pre-stellar gas clouds using numerically determined density and temperature profiles for the clouds. Where those works determined the 'critical' (marginally stable) central density of gas cores of fixed mass, we undertake a dynamical model of the collapse based on a sequence of marginally stable cores. The details of the implementations also differ: where those works determined the density and temperature profiles using an iterative procedure involving 1D radiative transfer, we employ an effective barotropic equation of state generated by a one-zone calculation. Then, we determine the density and temperature profile by numerically solving a sequence of ordinary differential equations.

We also mention the recent work of Smith et al. (2024), which illustrates the importance of radiative cooling in controlling the onset of gravitational instability by demonstrating a critical gas-phase metallicity for star formation in strong ultraviolet backgrounds. That work uses a combination of 3D simulations and one-zone modelling. In the one-zone model, the density and temperature can be understood as average values. Gravitational collapse (and thus star formation) is assessed to begin when the one-zone density and temperature indicate instability via the isothermal Bonnor–Ebert criterion. Here, we develop an MBE condition, which can account for temperature/pressure gradients as well as the contribution of dark matter to the gravitational potential. Based on this Bonnor–Ebert criterion, we build up a 1D model of the dynamics of the collapse and show that the onset of instability can be understood through the thermal evolution of the gas. We explain the qualitative agreement between our model (in which the gas core is never unstable) and mean density-based calculations such as that of Smith et al. (2024) in Appendix D.

Our approach is tractable in large part due to the powerful tools provided by the SciML ecosystem (Rackauckas & Nie 2017) for solving and analyzing differential equations.

This paper is organized as follows. In Section 2, we develop the model using the canonical example of a mini-halo cooled by molecular hydrogen. Subsequently, we apply these methods to two further examples in Section 3. In Section 3.1, we consider the case where a delayed collapse leads to the formation of HD which delays gravitational instability to higher density and smaller mass. In Section 3.2, we consider the opposite case, where the gas heats up to the point that atomic cooling is efficient. There, the nearly isothermal equation of state leads to prompt gravitational collapse. We close with a summary of the main results and brief discussion of directions for future research.

2 METHOD

We begin by explicating the model using the example of a mini-halo cooled by molecular hydrogen, before turning to further examples in the next section. The steps of the calculation are as follows. We first generate an effective barotropic equation of state for the gas using a one-zone calculation (Section 2.1), and then apply this equation of state to compute a radial density profile valid in the inner, pressure-supported part of the cloud, which we first use to generalize the Bonnor–Ebert stability condition and apply this condition to calculate the full density profile of the gas (Section 2.2). We discuss the gravitational stability of this density profile by calculating the ratio of the mass enclosed to the Bonnor–Ebert mass and, in Section 2.3, by calculating the time-dependent mass accretion from the envelope on to the core.

2.1 The effective equation of state

Our model requires an effective equation of state as an input. Here, we calculate this equation of state using the density–temperature relationship determined from a one-zone model. This equation of state could also in principle be determined by time-scale arguments (e.g. Chang et al. 2019; Bramante et al. 2024b), or from the density–temperature relationship in marginally resolved structures in a hydrodynamical simulation. The underlying logic is that due to the self-regulatory behaviour of the thermal evolution (discussed below) even a simple ansatz for the density evolution can produce a reasonably accurate density–temperature relationship and hence effective equation of state, which we will here build into a more accurate dynamical model. We begin by briefly explicating the one-zone model, and refer the reader to, for example, Gurian et al. (2024) for more detailed discussion. The temperature evolution of a uniform density parcel of gas (say, in the core of a gas cloud) is given as

$$\frac{{\rm d}T}{{\rm d}t} = (\gamma - 1)\left[\frac{\dot{n}}{n}T - \frac{\mathcal{C}(T, \vec{n})}{k_{\rm B} n}\right], \tag{2}$$

Downloaded from https://academic.oup.com/mnras/article/537/1/580/7943696 by guest on 09 March 2025

Table 1. The initial fractional abundances and their sources.

Species	Initial abundance	Source
x_e	2.5×10^{-4}	RECFAST (Seager, Sasselov & Scott 1999)
x_{H_2}	7×10^{-7}	Hirata & Padmanabhan (2006)
x_D	2.5×10^{-5}	Cooke, Pettini & Steidel (2018)
x_{D+}	6.3×10^{-9}	$x_{D+}/x_D \equiv x_{H+}/x_H$
x_{HD}	1.8×10^{-11}	$x_{HD}/x_D \equiv x_{H_2}/x_H$

with γ is the adiabatic index, n is the total number density, T is the temperature, $\mathcal{C}$ is the volumetric cooling rate and $\vec{n}$ is the number densities of the various species. Evaluating this equation at a given density requires the chemical composition $\vec{n}$ and the time derivative of the density. The former can be supplied by solving a chemical network (i.e. a system of ordinary differential equations describing the interconversion of the various species). However, calculating $\dot{n}$ requires the full dynamics of the gas, including gravitation and pressure. These dynamics can (at considerable computational cost) be supplied by hydrodynamical simulations. Instead, we apply a simple ansatz the density in our gas parcel evolves on some characteristic collapse time-scale:

$$\dot{\rho} = \frac{\rho}{t_{\rm col}}. \tag{3}$$

Under this assumption, we can numerically integrate equation (2) together with the chemical network and determine T as a function of ρ alone. Note that equation (2) can be rewritten as (Gurian et al. 2024)

$$\frac{\mathrm{d}\log T}{\mathrm{d}\log n} = (\gamma - 1)\left[1 - \frac{t_{\rm col}(n)}{(\gamma - 1)t_{\mathcal{C}}(\vec{n}, T)}\right], \tag{4}$$

which demonstrates a self-regulatory behaviour of the gas, in that over the course of the collapse the temperature will adjust so that $t_{\rm col}(n) \approx (\gamma - 1)t_{\mathcal{C}}$.

For the example molecular cooling mini-halo, we adopt the initial abundances described in Table 1 and solve a standard chemical network using KROME (Grassi et al. 2014) with the initial temperature and density set appropriate to a $5 \times 10^5\,\mathrm{M}_\odot$ halo at $z = 25$, taking $t_{\rm col} = t_{\rm ff}$, with the free-fall time-scale defined by

$$t_{\rm ff} = \sqrt{\frac{3\pi}{32G\rho}}. \tag{5}$$

Throughout this work, we will take $t_{\rm col} = t_{\rm ff}$ (in this example and in Section 3.2) or $t_{\rm col} = f t_{\rm ff}$ (in Section 3.1), with f a constant, here effectively a free parameter. We discuss this choice and the possibility of time-varying f in Appendix A. The resulting density–temperature relationship is shown in Fig. 1. At low densities and temperatures, the cooling is not yet efficient and the gas evolves by adiabatic heating. The first local maximum of the temperature is the intersection of the thermal trajectory of the gas with the curve $t_{\rm col}(n) \approx (\gamma - 1)t_{\mathcal{C}}$. This marks the beginning of the cooling-regulated core contraction, and is closely related to the Rees–Ostriker condition. The difference is that we allow $t_{\rm col}$ to vary by an overall, order unity factor from $t_{\rm ff}$, which is an approximate treatment of any slowdown in the evolution due, for example, to temporarily ineffective cooling or rotational support. This runaway contraction on a time-scale comparable to $t_{\rm ff}$ continues until thermal pressure overcomes the gravitational force, when the adiabatic index $\mathrm{d}\ln p/\mathrm{d}\ln\rho > 4/3$ (e.g. Omukai et al. 2005). In the remainder of this work, we do not consider the initial, heating part of the trajectory. We integrate the chemical–thermal network until the central density reaches $10^{13}\,\mathrm{cm}^{-3}$, a number chosen somewhat arbitrarily but far larger than the 'loitering point' which is our primary interest.

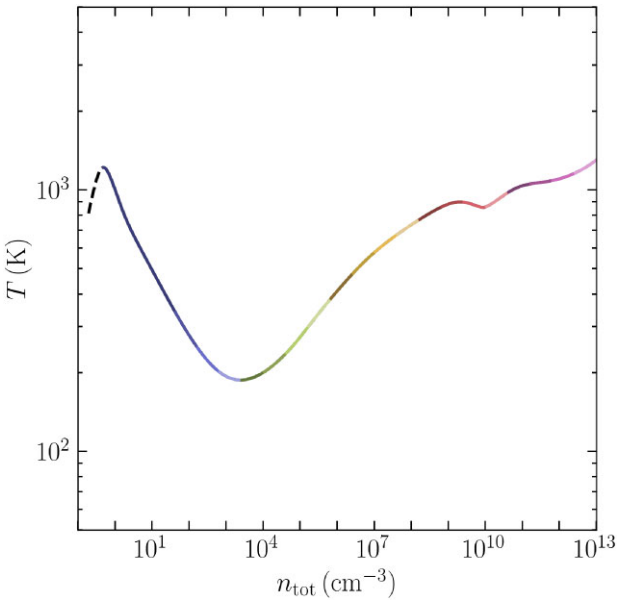

Figure 1. The one-zone temperature–density relationship for a $5 \times 10^5\,\mathrm{M}_\odot$ halo at $z = 25$ collapsing on the free-fall time-scale. The black, dashed part of the curve is the initial, adiabatic heating up to the point where $t_{\rm col} \sim t_{\mathcal{C}}$. The cooling part of the curve is colour-coded for easy identification with subsequent figures.

2.2 Density profile and Bonnor–Ebert mass

Based on this density–temperature relationship, we wish to calculate a radial density profile. The guiding intuition is that for any given central density and temperature, the radius of the gas core is of the order of the local Jeans length. Further, the collapse is highly non-homologous in the sense that the density far from the core hardly changes as the central density increases. Therefore, we can sketch a density profile by conceptually inverting

$$r = \lambda_{\rm J}(\rho, T(\rho)), \tag{6}$$

with $\lambda_{\rm J}$ is the Jeans length. In this section, we develop this intuition using an MBE scale.

2.2.1 The core profile

In the inner 'core' region, we determine the density profile by numerically integrating the equation of hydrostatic equilibrium. This is reasonable because even in the presence of efficient radiative cooling, pressure can regulate the collapse on small scales. In other words, sufficiently deep in the gas core, the sound crossing time is short compared to the evolutionary time-scale. We will shortly determine the threshold where the quasi-hydrostatic evolution breaks down, which is the Bonnor–Ebert scale. Now, in spherical symmetry, the equation of hydrostatic equilibrium is

$$-\frac{G\left[M_{\rm DM}(r) + M(r)\right]\rho}{r^2} = \frac{\mathrm{d}P}{\mathrm{d}\rho}\frac{\mathrm{d}\rho}{\mathrm{d}r}, \tag{7}$$

where $M_{\rm DM}$ is the dark matter mass, M is the gas mass, ρ is the gas density, and the pressure is P and its derivative are supplied by the

Downloaded from https://academic.oup.com/mnras/article/537/1/580/7943696 by guest on 09 March 2025

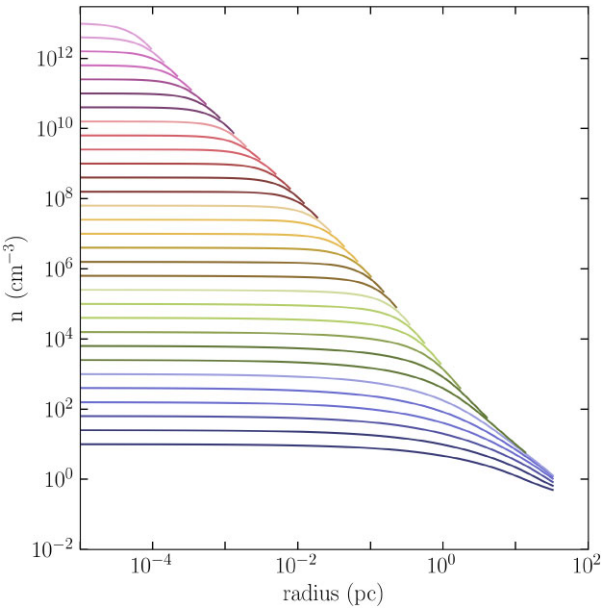

Figure 2. The hydrostatic density profiles out to the minimum of the Bonnor–Ebert radius or the initial values of n, T in Fig. 1, for a range of central densities. The central density for each curve is colour-coded to correspond with Fig. 1.

effective barotropic equation of state

$$P(n) = nk_{\rm B}T(n). \tag{8}$$

Equation (7) can be integrated numerically along with the equation of mass conservation

$$\frac{{\rm d}M_{\rm tot}}{{\rm d}r} = 4\pi r^2\left[\rho(r) + \rho_{\rm DM}(r)\right], \tag{9}$$

where $M_{\rm tot} = M_{\rm DM} + M$, and we are neglecting the effect of the gas evolution on the dark matter (though see Spolyar, Freese & Gondolo 2008). In our molecular cooling mini-halo, we take a dark matter density profile informed by the simulations of Hirano et al. (2014), which generated a sample of ~ 100 clouds collapsing in haloes of masses between 10^5 and $10^6\,{\rm M}_\odot$ and at redshifts between $10 \lesssim z \lesssim 35$. The dark matter density profiles found in that work can be approximated by (Hirano private communication),

$$\rho_{\rm DM}(r) = \frac{\sqrt{2}\rho_{\rm s}}{\left(\frac{r}{r_{\rm s}}\right)^{3/2}\left(1+\frac{r}{r_{\rm s}}\right)^{1/2}}, \tag{10}$$

with $\rho_{\rm s} = 5m_{\rm H}\,{\rm cm}^{-3}$, where $m_{\rm H}$ is the mass of the hydrogen atom and $r_{\rm s} = 30\,{\rm pc}$. The parameters $\rho_{\rm s}$ and $r_{\rm s}$ should in principle depend on the halo mass and redshift, and at a given radius the density can vary by a factor of ~ 10 over the simulation suite. We discuss the sensitivity of our results to the dark matter density in Appendix C.

With $\rho_{\rm DM}$ set, we can numerically integrate equations (7)–(9) from any assumed central density $\rho_{\rm c}$. The result is the hydrostatic radial density profile of the gas, $\rho_{\rm HSE}(\rho_{\rm c}, r)$. At large radii, the hydrostatic density profile can represent an unstable equilibrium. The transition from stable to unstable equilibrium is defined by the Bonnor–Ebert scale. In Fig. 2, we plot the hydrostatic density profile out to whichever is less of the MBE radius (defined below) or the initial temperature maximum of the density–temperature relationship (where $t_{\rm col} \sim t_C$, which also defines a cooling radius for the gas $r_{\rm C}$[1]).

2.2.2 The Bonnor–Ebert mass

In the standard treatment of gravitational instability (in which radiative losses are neglected) excessively centrally concentrated density profiles are unstable to collapse and fragmentation while less concentrated profiles can remain indefinitely hydrostatic. The picture is different for gases which lose kinetic energy through radiation. Such clouds can quasi-hydrostatically contract to higher central densities regardless of the presence or absence of a perturbative instability. In this case, both the cooling (or Kelvin–Helmholtz) and free-fall time-scales are decreasing functions of density. This results in a tendency for the dense, inner regions of a cloud to 'run away' to still higher densities on the relevant local time-scale.

For such a collapsing central region in a (quasi-)static external medium, a Bonnor–Ebert stability criterion applies. Consider a central region of the cloud infinitesimally contracting to a new hydrostatic configuration on its local Kelvin–Helmholtz time-scale. If this contraction leads to an increase in surface pressure, sound waves will push the gas back towards its original configuration. On the other hand, if the surface pressure decreases then the gas will be accelerated towards the centre of the cloud.

Exact contraction on the local Kelvin–Helmholtz time-scale corresponds to marginal Bonnor–Ebert stability,

$$\left(\frac{\delta P}{\delta V}\right)_M = 0, \tag{11}$$

which is the classical Bonnor–Ebert condition that applies to spherical gas clouds of fixed mass (Ebert 1955; Bonnor 1956). However, the Bonnor–Ebert mass (like the Jeans mass) is usually a decreasing function of central density. This means that in the case of the contracting gas core, we should no longer hold the mass fixed. Thus, we consider instead the surface pressure response to an increase in central density, at fixed radius:

$$\frac{\delta P}{\delta \rho_{\rm c}} = \left.\frac{\partial P}{\partial \rho}\right|_{\rho=\rho_{\rm HSE}} \frac{\partial \rho_{\rm HSE}}{\partial \rho_{\rm c}} = 0, \tag{12}$$

which defines the radius/density at which contraction proceeds in pressure equilibrium. For the HSE case that we show in Fig. 2, $\rho_{\rm c}$ is one to one to the size of the core. As long as $\frac{\partial P}{\partial \rho}$ does not change sign,[2] the first zero of this quantity occurs when

$$\frac{\partial \rho_{\rm HSE}}{\partial \rho_{\rm c}} = 0. \tag{13}$$

Equation (13) defines the MBE radius throughout the rest of this work. In Appendix B, we explicitly relate this condition to the standard Bonnor–Ebert condition, equation (11). Note that equation (13) in fact requires calculating the derivative of a numerical solution to an ordinary differential equation with respect to its initial condition. This is readily accomplished using the sensitivity analysis tools provided as part of the SciML ecosystem (Rackauckas et al. 2020).

[1]We point out that this $r_{\rm C}$ differs conceptually from the cooling radius of, for example, Bertschinger (1989), which is based on the age of the system rather than its dynamical time-scale.

[2]In fact, as $\frac{\partial P}{\partial \rho} \to 0$, the sound speed also goes to zero, promoting the development of shocks and a breakdown of our treatment. In all the cases considered here $\frac{\partial P}{\partial \rho} > 0$.

Downloaded from https://academic.oup.com/mnras/article/537/1/580/7943696 by guest on 09 March 2025

As long as the cooling time-scale is a decreasing function of density, during the contraction the outer regions of the cloud can never 'catch up' to the contracting core. That is, the evolution of the inner part of the cloud is approximately independent of the outer part. The MBE condition equation (13) sets the scale at which the central region of the gas cloud decouples from its surroundings and escapes to high densities via radiative cooling.

Associated with the MBE radius $r_{\rm MBE}$ is the Bonnor–Ebert mass. Defining $\rho_{c,\rm MBE} \equiv \rho_c(r_{\rm MBE})$ as the central density for which the Bonnor–Ebert radius is $r_{\rm MBE}$,

$$M_{\rm MBE} = 4\pi \int_0^{r_{\rm MBE}} r^2 {\rm d}r\, \rho_{\rm HSE}(\rho_{c,\rm MBE}, r), \tag{14}$$

which is the largest possible stable, hydrostatic mass enclosed in the Bonnor–Ebert radius $r_{\rm MBE}$, consistent with the effective barotropic equation of state of the gas.

2.2.3 *The envelope and cloud mass*

At a given central density $\rho_{\rm c}$ and for $r \leq r_{\rm MBE}(\rho_{\rm c})$, we calculate the density profile by solving the equation of hydrostatic equilibrium, equation (7):

$$\rho(r) = \rho_{\rm HSE}(\rho_{\rm c}, r). \tag{15}$$

For $r > r_{\rm MBE}(\rho_{\rm c})$, we calculate the density as the hydrostatic equilibrium density at that radius when $r_{\rm MBE} = r$ (that is, at some previous time when $\rho_{\rm c} = \rho_{c,\rm MBE}$):

$$\rho(r) = \rho_{\rm MBE}(r) \equiv \rho_{\rm HSE}(\rho_{c,\rm MBE}, r). \tag{16}$$

In other words, we assume that the density at $r(> r_{\rm MBE})$ has not evolved since the earlier time/lower central density where r was the Bonnor–Ebert radius. The assumption is reasonable because when $\rho_{\rm c} \approx \rho_{c,\rm MBE}$ the density at r must be slowly evolving by equation (13), while once the central density has increased such that $\rho_{\rm c} \gg \rho_{c,\rm MBE}$ the central evolutionary time-scale is very short compared to the evolutionary time-scale at $r_{\rm MBE}$. Then, the full density profile is

$$\rho(\rho_{\rm c}, r) = \begin{cases} \rho_{\rm HSE}(\rho_{\rm c}, r) & r \leq r_{\rm MBE}(\rho_{\rm c}) \\ \rho_{\rm MBE}(r) & r > r_{\rm MBE}(\rho_{\rm c}). \end{cases} \tag{17}$$

In practice, we determine the density profile for $r > r_{\rm MBE}$ by calculating the hydrostatic density profiles and Bonnor–Ebert radii over a grid of central densities, then splining through the hydrostatic density profiles at the Bonnor–Ebert radius of each. This is illustrated in Fig. 3. In the inner region, the profile agrees closely with that derived from the 1D hydrodynamic calculations of Omukai et al. (2010). Although that work did not include dark matter, we show in Appendix C that the effect of the dark matter on the density profile is minor in this inner region. Further, in Appendix E, we compare the model with 3D simulations. The slope is also consistent with the Larson–Penston polytropic solution for a gas with adiabatic index $\gamma \approx 1.1$ (which here holds between $10^4 \lesssim n \lesssim 10^7\,{\rm cm^{-3}}$) (Omukai & Nishi 1998a). Below this density, the Larson–Penston solution predicts a shallower density profile, which is not seen here due to the dark matter dominating the density at large radii (see Appendix C).

Given these density profiles, for any central density and radius, we can calculate the ratio of the mass enclosed to the Bonnor–Ebert mass,

$$\kappa_{\rm MBE} = \frac{M(r)}{M_{\rm MBE}(r)}, \tag{18}$$

for any r inside of the cooling radius ($r \leq r_{\rm C}$).

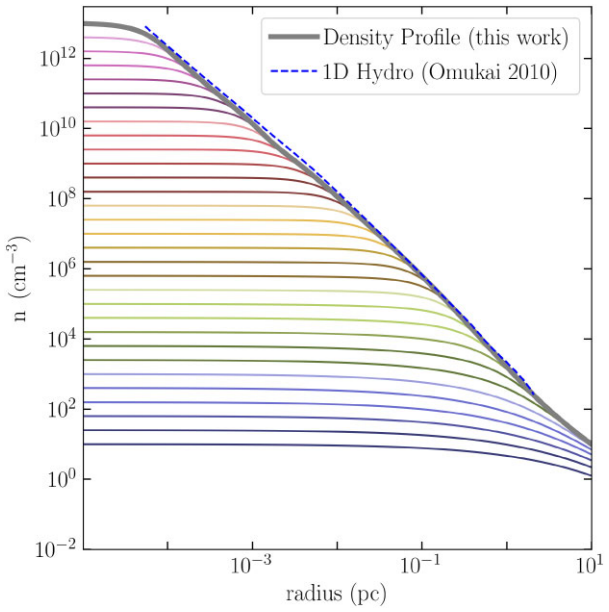

Figure 3. As Fig. 2, but we have now overplotted in grey the full density profile (equation 17) when the central density is $10^{13}\,{\rm cm^{-3}}$, as well as the late-time density profile from the 1D simulations of Omukai et al. (2010), here truncated at $10^{13}\,{\rm cm^{-3}}$. The agreement is quite close.

When $\kappa_{\rm MBE} < 1$ for all $r \leq r_{\rm C}$, the gas evolves on a global time-scale. If the low-density gas (i.e. the gas beyond $r_{\rm C}$) is adiabatically falling on to the core, this global time-scale may still be comparable to the free-fall time-scale. On the other hand, if the surrounding medium is nearly hydrostatic the time-scale may be considerably longer.

As soon as $\kappa_{\rm MBE}$ reaches unity within $r_{\mathcal{C}}$, the Bonnor–Ebert core begins to contract on its cooling time-scale, with $t_{\mathcal{C}} \sim t_{\rm ff}$. That is, a refined Rees–Ostriker criterion is given by

$$\kappa_{\rm MBE}(r_{\mathcal{C}}) = 1. \tag{19}$$

As the central density increases and the Bonnor–Ebert radius decreases the cooling and free-fall time-scales become shorter still: a period of runaway Kelvin–Helmholtz contraction begins. Throughout this phase, the density profile in the contracting core remains stable and nearly hydrostatic ($\kappa_{\rm MBE} \leq 1$). The contraction begins to decelerate once the gas can no longer radiate its gravitational energy within a free-fall time such that the equation of state becomes stiff with ${\rm d}\log P/{\rm d}\log\rho > 4/3$, for example, after becoming optically thick (Low & Lynden-Bell 1976; Rees 1976). By this point, the contraction of the core, which has proceeded nearly in equilibrium, has established a new density profile in the envelope. As we will establish quantitatively in the following Section (2.3), the amount by which $\kappa_{\rm MBE}$ exceeds unity at a given radius is related to the subsequent infall rate from the envelope on to the core: a larger value indicates more violent acceleration towards the core.[3]

The ratio $\kappa_{\rm MBE}$ in the molecular hydrogen-cooled cloud is shown in Fig. 4 for a range of central densities. We find that gravitational instability in the envelope sets in when the central density is near the molecular cooling critical density, $n_{\rm H} \sim 10^3\,{\rm cm^{-3}}$, and peaks around

[3]In fact, $\kappa_{\rm MBE}$ roughly tracks $t_{\rm ff}(n(r))/\sqrt{r/a(r)}$, where $a(r)$ is the gravitational acceleration less the pressure gradient, equation (21), so that $\kappa_{\rm MBE}$ can be intuitively understood as the ratio of the uniform-density free-fall time-scale to the local infall time-scale.

Downloaded from https://academic.oup.com/mnras/article/537/1/580/7943696 by guest on 09 March 2025

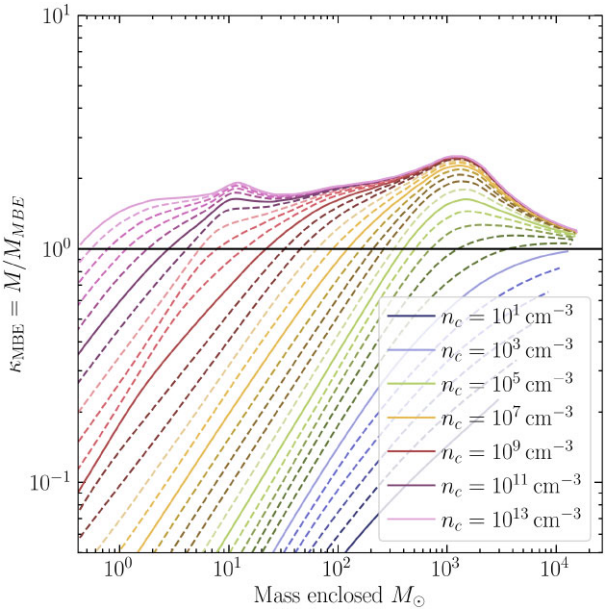

Figure 4. The ratio $\kappa_{\rm MBE}$ of mass enclosed to Bonnor–Ebert mass for a sequence of central densities, in the molecular cooling mini-halo. Gravitational instability begins to occur with the central density near the critical density of molecular hydrogen cooling ($n_c = 1000\,{\rm cm}^{-3}$), and $\kappa_{\rm MBE}$ peaks with $1000\,{\rm M}_\odot$ enclosed, corresponding to the Jeans mass at the loitering phase.

$1000\,{\rm M}_\odot$ (i.e. around the loitering point/mass). We also point out that Fig. 4 differs qualitatively from similar plots in the literature based on the isothermal Jeans mass (see Appendix D).

These results clarify the lore that a decreasing temperature (with density) 'promotes fragmentation' while an increasing temperature 'suppresses fragmentation' (e.g. Li et al. 2003). While we do not study the multiplicity of cores, our results illustrate how the characteristic mass of collapsing clouds depends on the density–temperature relationship. As illustrated by the light blue/dark green lines in Fig. 3, we see that once $\kappa_{\rm MBE}$ exceeds unity, a positive temperature gradient (i.e. strong cooling) leads to a shallow density profile (for $r \gtrsim 1$ pc) so that $\kappa_{\rm MBE}$ hardly increases in the envelope.[4] If the cooling were to continue indefinitely, the final result would be an infinitesimal core surrounded by a nearly hydrostatic envelope. It is plausible that this nearly hydrostatic outer region (with $M(r) \sim 10^4$ M$_\odot$) could be vulnerable to, for example, turbulent fragmentation leading to the formation of multiple contracting cores. In this picture, though, fragmentation is not invoked to explain the characteristic mass of these cores. On the other hand, an isothermal or heating density/temperature relationship (negative temperature gradient) leads to a prompt increase in $\kappa_{\rm MBE}$, so that nearly all of the core mass at the density where the isothermal/heating part of the evolution begins is rapidly accelerated inwards, here within $M(r) \lesssim 10^3$ M$_\odot$. These points are further illustrated in the examples of the following sections.

We emphasize again that this picture is quantitatively similar to but qualitatively distinct from the 'dynamical collapse' investigated by e.g. Larson (1969), Penston (1969), and Foster & Chevalier (1993).

[4]The maximum of $\kappa_{\rm MBE}$ also increases in the range $10 \lesssim n \lesssim 10^3\,{\rm cm}^{-3}$ despite the positive temperature gradient because $\kappa_{\rm MBE}$ has not yet exceeded unity. In this phase, an initial Bonnor–Ebert mass of gas is accumulating in the core.

Rather than setting up an isothermal gas cloud out of dynamical equilibrium, we are tracking the evolution of the cloud between quasi-equilibrium states determined by the gas chemistry and cooling rates. Without cooling, the gas would rapidly heat and the contraction stall out. In this sense, the contraction of the core is always regulated by pressure and cooling. While an isothermal equation of state can provide a reasonable approximation to this balance between cooling and heating, our approach clarifies the picture by more accurately including the underlying thermochemistry of the collapsing gas.

In particular, we point out that calculations involving self-gravitating isothermal gases do not conserve the total energy of the system: There is an implicit energy loss rate imposed by the equation of state. Unlike realistic radiative cooling rates, the isothermal energy loss rate (which is just the opposite of the compressional heating term) is a function only of $\dot{\rho}$, which is why isothermal runaway collapse is initiated from rest only when the configuration is already dynamically unstable.

Finally, on a practical note, we point out that the MBE scale can be assessed in two ways in simulations. First, $r_{\rm MBE}$ can be determined as the point where the density stays stationary in successive snapshots. Alternatively, the thermal evolution determined from the simulation can be used as the input in this model to determine the MBE radius as a function of central density, and in turn $\kappa_{\rm MBE}$ (see Appendix E).

2.3 Infall rate

We now explain the implications of $\kappa_{\rm MBE} > 1$ for the dynamics of the gas, by using the density and velocity profiles before protostar formation to estimate the infall rate after the contraction halts and a hydrostatic core is formed. The conceptual point is that for $\kappa_{\rm MBE} > 1$, the density is larger than the hydrostatic value, and the gas is thus accelerated towards the core. A widely adopted estimate of the infall rate (e.g. Hosokawa & Omukai 2009; Li, Inayoshi & Qiu 2021) is

$$\dot{M} \approx M_{\rm J}/t_{\rm ff} \approx c_{\rm s}^3/G. \tag{20}$$

In the Larson–Penston solution (which represents a highly dynamical isothermal collapse), $\dot{M} \approx 47 c_{\rm s}^3/G$ (Hosokawa & Omukai 2009), while in the initially static Shu solution, the prefactor is very nearly unity (Shu 1977). Neither limit is typically attained in simulations (e.g. Hunter 1977; Foster & Chevalier 1993; Omukai et al. 2010), where (in contrast to the Larson–Penston solution) the initially small infall velocity at large radii is relevant and (in contrast to the Shu solution) the envelope is not hydrostatic at the end of the core contraction phase. Moreover, these similarity solutions do not account for the departures from isothermality, which introduce new scales in the problem.

Towards a calculation of the infall rate, we estimate the radial velocity profile of the gas once the core has become small and dense (near the epoch of protostar formation) using the density profile calculated above. We model the radial velocity profile from the trajectory of a test particle moving towards the centre of the cloud, assuming that significant gravitational acceleration is sourced at the radius r only once the core contracts to much smaller radii.

In this test-particle model, we approximate the acceleration field as constant in time but varying in space. The acceleration experienced at each radius r is thus given as the gravitational acceleration from the late-time mass enclosed less the pressure gradient:

$$\frac{{\rm d}v}{{\rm d}t} = -\frac{G[M_{\rm DM}(r) + M(r)]}{r^2} - \frac{1}{\rho}\frac{{\rm d}P}{{\rm d}\rho}\frac{{\rm d}\rho}{{\rm d}r}, \tag{21}$$

where $M_{\rm DM}(r)$ is the dark matter mass interior to r (which is assumed not to evolve over the collapse) and $M(r)$ is the late-time mass

Downloaded from https://academic.oup.com/mnras/article/537/1/580/7943696 by guest on 09 March 2025

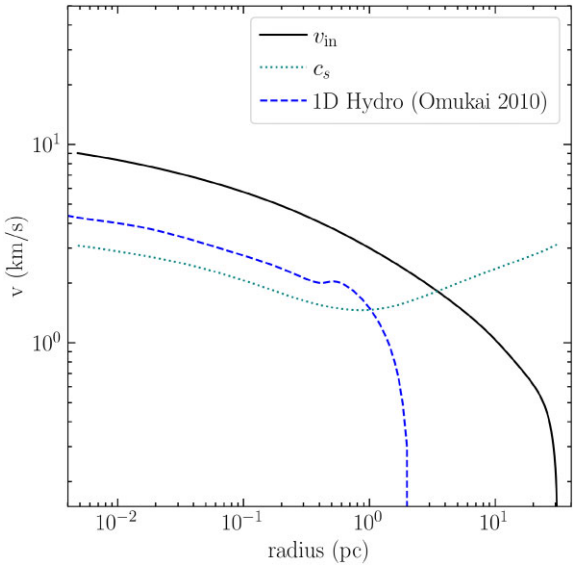

Figure 5. The radial velocity profile for the molecular cooling mini-halo (solid, black), along with the sound speed (teal, dotted) and the velocity profile found by Omukai et al. (2010) (blue, dashed). The disagreement at large radii is due to the imposition of a zero-velocity boundary condition around 2 pc in Omukai et al. (2010). However, a factor of (almost exactly) 2 discrepancy persists in the inner region.

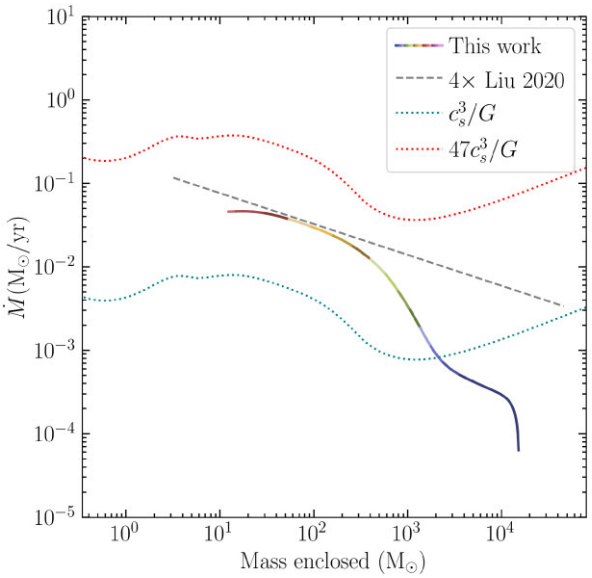

Figure 6. The infall rate as a function of mass enclosed for the molecular cooling mini-halo (solid, multicoloured), along with the Shu quasi-static accretion rate (teal, dotted), the Larson–Penston accretion rate (red, dotted), and quadruple the semi-empirical fit of the protostellar accretion rate from Liu et al. (2021) (grey, dashed). The colour is related to the mass through $M(r(n))$ in the late-time density profile, with the mapping from colour to density as in Fig. 1. Note the pronounced dropoff in the accretion rate past the loitering point. For the accretion rates appropriate to the similarity solutions, the position on the horizontal axis is calculated as the Jeans mass at each (n, T).

enclosed (in this example, the mass enclosed when the central density is $10^{13}\,{\rm cm}^{-3}$).

That is, using the identity $dv/dt = v dv/dr = \frac{1}{2}d(v^2)/dr$, we integrate the equation as

$$v^2(r) - v^2(r_i) = 2\int_{r_i}^{r} dr \left[-\frac{G[M_{\rm DM}(r) + M(r)]}{r^2} - \frac{1}{\rho}\frac{dP}{d\rho}\frac{d\rho}{dr}\right]. \quad (22)$$

We do not model in detail the drop-off of the infall velocity near the core. Instead, we truncate the velocity profile at 25 times the Bonnor–Ebert radius at the highest central density in our calculation. We impose a zero-velocity boundary condition and begin the integration when the mass enclosed first exceeds the Bonnor–Ebert mass. The assumption that the gas is accelerated from near rest is most reasonable if there is an initial quasi-static period, for example, as coolants accumulate.[5] However, we have checked that the results in the inner region are insensitive to this assumption (see Appendix C). Therefore, we are justified in beginning the integration at the radius R_0 where the following condition is satisfied:

$$t_{\rm in} = \sqrt{-R_0/a(R_0)} < 10^7\,{\rm yr}, \quad (23)$$

with the acceleration $a(R_0)$ given by the right-hand side of equation (21). By this condition, we avoid the situation that immediately after exceeding the Bonnor–Ebert mass equation (21) can be very stiff.

The velocity profile is shown in Fig. 5. Our velocity profile initially (i.e. at large radii) greatly exceeds the results of Omukai et al. (2010) because those authors imposed a zero velocity boundary condition at a smaller radius. In the inner region, our velocity exceeds the 1D hydro results by a factor of almost exactly 2, a discrepancy which persists even if we match the zero-velocity boundary condition to the hydro calculation. The disagreement can be explained by the fact that in our approximation that the gas at radius r is accelerated by the 'very' late time mass enclosed, rather than 'somewhat' after the Bonnor–Ebert radius becomes smaller than r. That is, in reality the right-hand side of equation (21) should evolve with time as the gas at r is accelerated over a window of times/central densities after the core has receded from r but before the central time-scale becomes too short to meaningfully affect the scale r.

Proceeding, we construct the infall rate as

$$\dot{M}(r) = 4\pi r^2 \rho v, \quad (24)$$

with v as calculated above and ρ is the late-time density profile.

The result is shown in Fig. 6, where we have adopted the late-time enclosed mass as the independent variable via $M = 4\pi\int dr\, r^2\rho$. This is an estimate based on the envelope structure of the cloud scale infall rate as a function of the mass fallen on to the disc. If the inefficiency of accretion of the protostar through the disc is neglected, this quantity can be interpreted directly as the protostellar accretion rate as a function of protostellar mass, as in (for example) Hosokawa & Omukai (2009). The peak in $\kappa_{\rm MBE}$ (Fig. 4) corresponds to a regime of rapidly increasing infall rate. At small masses our calculations roughly tracks the estimate equation (20), with an overall enhancement sourced during the early, highly gravitationally unstable phase of the collapse of the envelope. This is also approximately consistent with the analytic calculation of Tan & McKee (2004), although in that work a free parameter of the order of

[5]It is possible to estimate a non-zero initial velocity at the Bonnor–Ebert radius by considering virial equilibrium and/or dissipation of turbulent velocity of the cloud at larger/halo scales (McKee & Tan 2003; Luo, Liu & Li 2024a, b). Here, we adopt the simple zero-velocity condition in line with the canonical picture of monolithic collapse of primordial gas under inefficient cooling and weak turbulence (Chon, Omukai & Schneider 2021). It is shown in Appendix E that this assumption has minor effects on the mass scale and dynamics of collapse.

Downloaded from https://academic.oup.com/mnras/article/537/1/580/7943696 by guest on 09 March 2025

unity (corresponding to the enhancement relative to the Shu solution) multiplies the accretion rate. Our estimate is a factor of few greater than the semi-empirical estimate of the protostellar accretion rate of Liu, Meynet & Bromm (2021) in the regime where that fit was calibrated. The factor of few can be attributed to the inefficiency of accretion on to protostars through the accretion disc as compared with the cloud level infall rate, together with the factor of 2 overestimate of the velocity in our calculation.

We find important qualitative differences relative to the Jeans estimate equation (20), related to the arguments discussed in the preceding section. Crucially, we demonstrate that the infall rate depends not only on the sound speed, but also on its gradient. A sound speed which decreases with increasing density is associated with a *more* stable configuration (Fig. 4 and accompanying text) and a correspondingly smaller infall rate. In contrast, the Jeans estimate $\dot{M} \sim c_s^3/G$ depends on the temperature alone.

Now, we have obtained the relation between the infall rate $\dot{M}$, collapsed/enclosed mass M, and the corresponding cloud spatial (r) and density ($n \propto M/r^3$) scales, from which we can further derive their time evolution with $t(M) = \int_0^M [1/\dot{M}(M')]\mathrm{d}M'$. This is a crucial step towards predicting the final outcome of the collapse. Hydrodynamic simulations and analytical models show that due to the angular momentum of the infalling gas and outflows, only a fraction $\eta \sim 0.25 - 0.75$ (Matzner & McKee 2000; Sakurai et al. 2016; Tanaka, Tan & Zhang 2017; Staff, Tanaka & Tan 2019; Toyouchi et al. 2023) of the collapsed mass M is accreted by the protostars through a protostellar disc, whose size R is correlated with the collapsed mass M (Tan & McKee 2004; Liu et al. 2021). As shown in a companion paper Liu et al. (2024), the scaling relations $\dot{M}(M)$, $t(M)$, and $R(M)$, can be used to calculate the final mass of Pop III stars formed in the cloud with an analytical model that considers the balance between gas infall and disc photoevaporation by the ionizing photons from protostars, and the limit of stellar mass placed by lifetime and instability. Assuming $\eta = 0.5$ and only one protostar forms in the cloud for simplicity, applying our results to the model in Liu et al. (2024) produces a final stellar mass of $\hat{M}_\star \simeq 260\ \mathrm{M}_\odot$, consistent with the results from hydrodynamic simulations of H_2-cooling clouds with similar gas infall rates $\dot{M} \simeq 0.016\ \mathrm{M}_\odot\ \mathrm{yr}^{-1}$ at the density scale of $n \simeq 10^6\ \mathrm{cm}^{-3}$ (Hirano et al. 2014, 2015; Sugimura et al. 2023; Toyouchi et al. 2023).[6]

3 EXAMPLES

We now present two additional applications of the methods developed in the preceding sections, which further elucidate the relevant physics. First, we demonstrate a case where the collapse is delayed, allowing the efficient formation of HD. The resulting cooling and heating are then stronger due to the presence of HD, emphasizing the arguments we have developed. Secondly, we present a nearly isothermal atomic-cooling example, which is in a sense the opposite extreme.

[6]The original model in Liu et al. (2024) assumes a power-law scaling $\dot{M} \propto M^{-0.37}$ following Liu et al. (2021), which is valid for polynomial gas with $P \propto n^{1.09}$ (Omukai & Nishi 1998b; Tan & McKee 2004). In our case, the decline of $\dot{M}$ with M is more rapid for $M \gtrsim 100\ \mathrm{M}_\odot$, likely due to the zero-velocity boundary condition (at the moment when the mass enclosed first exceeds the Bonnor–Ebert mass, see Appendix C) and the deviation of the effective equation of state from a simple power-law. As a result, the final stellar mass predicted from our $\dot{M}(M)$ is lower than that from the power-law model in Liu et al. (2024) by a factor of ~ 2. This difference is within the scatter seen in the predictions of hydrodynamic simulations.

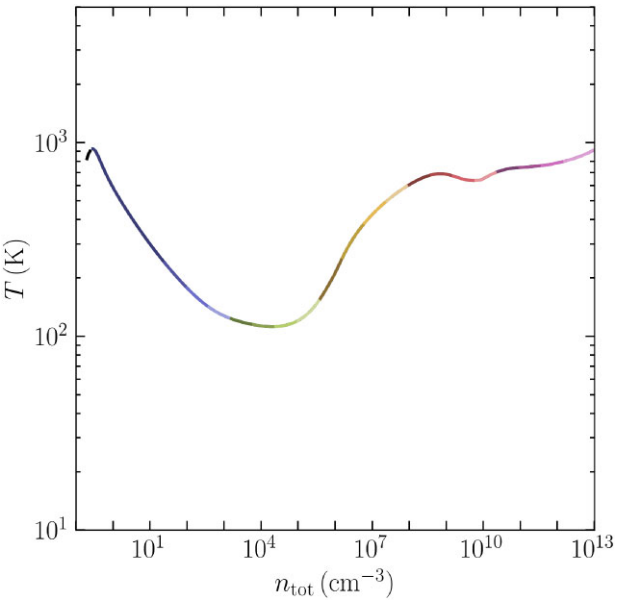

Figure 7. The temperature–density relationship for the delayed contraction, $t_{\mathrm{col}} = 3t_{\mathrm{ff}}$. A lower minimum temperature and steeper temperature gradients are realized due to the production of HD.

3.1 Delayed core contraction with the HD molecule

If the contraction of a pristine gas cloud's core is delayed, for example, due to rotation (Hirano et al. 2014) or an initial shortage of coolants (Gurian et al. 2024), the chemical thermal-evolution is modified due to chemical fractionation of the HD molecule. We now apply our model to explain how this modification of the chemistry propagates into the dynamics of the collapse. To this end, we adopt initial conditions exactly as in the previous section except that we take $t_{\mathrm{col}} = 3t_{\mathrm{ff}}$. It is not completely straightforward to set up a hydrodynamical simulation with realistic initial conditions which guarantee that $t_{\mathrm{col}} = 3t_{\mathrm{ff}}$. However, we have shown in Gurian et al. (2024) that in the simplest case of Pop. III star formation (neglecting, for example, Lyman–Werner backgrounds, turbulence, and the baryon dark matter streaming velocity) the delay factor can be predicted based on the host halo mass and redshift. We demonstrate in this section how such knowledge of the thermal evolution of the core can be directly extended into predictions concerning the dynamics of the collapse. Extending the calculation of the delay factor to include additional environmental factors is a target for future work.

The temperature–density relationship for this case is shown in Fig. 7. Compared to the H_2 cooling example shown in Fig. 1, the minimum temperature here is lower, $\sim 70\,\mathrm{K}$. Using this density–temperature relationship and equation (17), we compute the density profile shown in Fig. 8. Note that owing to the steeper temperature gradients, the density profile exhibits stronger features than that of the H_2 cooling example shown in Fig. 3.

We show the ratio κ_{MBE} in Fig. 9. Compared to the H_2 cooling halo case (Fig. 4), κ_{MBE} first exceeds unity only somewhat later, when the central density is around $10^4\ \mathrm{cm}^{-3}$. However, κ_{MBE} stays close to one until the central density increases past $10^6\ \mathrm{cm}^{-3}$, which is because the temperature changes only modestly between $\sim 10^3$ and $\sim 10^5\ \mathrm{cm}^{-3}$. Beyond this point, the rapidly increasing temperature causes κ_{MBE} to rapidly increase. In fact, the temperature increases sharply enough that M_{MBE} briefly increases with density, so that the κ_{MBE} curves cross each other in the inner region. The eventual result is a sharp peak in κ_{MBE} near $200\,\mathrm{M}_\odot$.

Downloaded from https://academic.oup.com/mnras/article/537/1/580/7943696 by guest on 09 March 2025

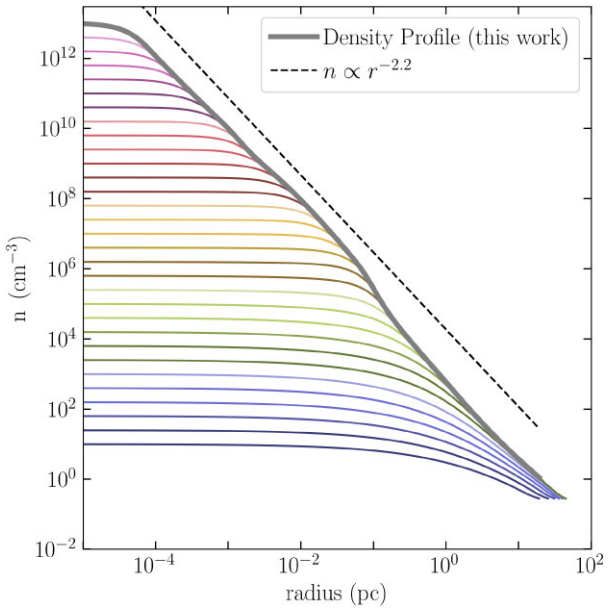

Figure 8. As Fig. 3, but for the delayed contraction with HD cooling. Here, lacking a reference hydro run we have simply overplotted the characteristic $n \propto r^{-2.2}$ slope. Note the more pronounced features in the density profile due to stronger deviations from isothermality.

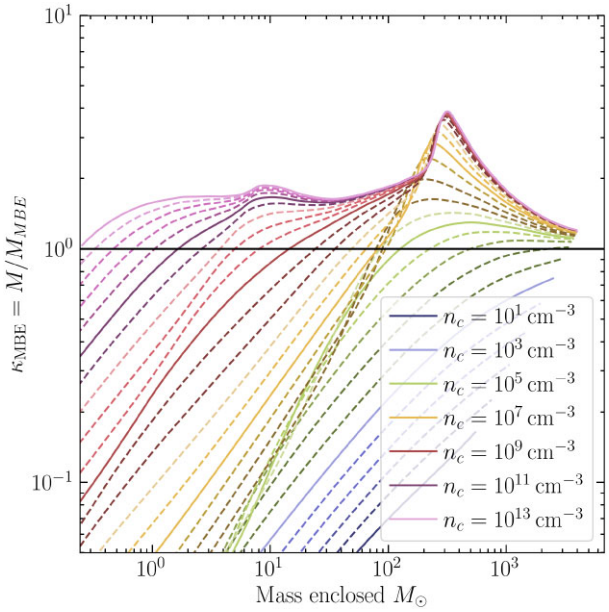

Figure 9. As Fig. 4, but for the delayed contraction with HD cooling. Gravitational instability in the envelope is established when the temperature begins to rise.

The fact that $\kappa_{\rm MBE}$ remains very close to unity for the initial part of the collapse (due to the strong cooling) means that as the central density increases the envelope remains nearly hydrostatic. The resulting accretion rate is shown in Fig. 10. In this case, the c_s^3/G estimate becomes ill-defined due to the non-monotonicity of both Bonnor–Ebert mass and Jeans mass, mentioned above.

The results of this section are qualitatively consistent with the simulations of, for example, Hirano et al. (2014) and Nishijima et al. (2024), as discussed in detail in Appendix E. Omukai et al. (2010)

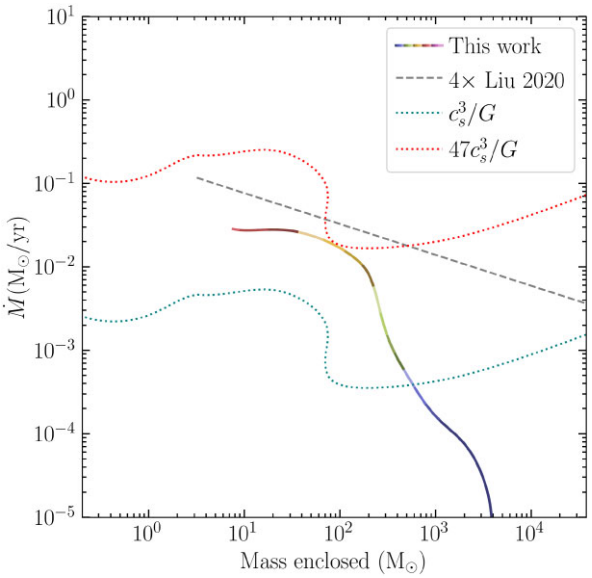

Figure 10. The accretion rate as Fig. 6, but for the delayed collapse with HD cooling. Due to the strong heating, once HD is destroyed, the mapping from $(n, T(n))$ to the Jeans mass (which is used to define the mass coordinate in the c_s^3/G estimates) is no longer one to one.

also provide a benchmark for the effects of varying thermal evolution on the infall rate. The same trends of positive temperature gradients (cooling) leading to decreased infall rates while heating leads to sharply increasing infall rates are seen also in that work. However, a sharp dropoff in the infall rate is seen only at the zero-velocity boundary condition, because in that case the initial conditions were already gravitationally unstable. As expected, the infall rate is lower ($\dot{M} \simeq 0.0092\,{\rm M}_\odot\,{\rm yr}^{-1}$ at $n \simeq 10^6\,{\rm cm}^{-3}$) compared with the standard H_2-cooling case shown in Fig. 6, resulting in a lower final stellar mass $\hat{M}_\star \simeq 120\,{\rm M}_\odot$ according to the analytical model in Liu et al. (2024).

3.2 Atomic-cooling halo

If the formation of molecular hydrogen is inhibited (for example by dynamical heating due to frequent mergers, collisional dissociation, or a strong Lyman–Werner background; Omukai 2001; Latif et al. 2013; Wise et al. 2019; Kiyuna et al. 2023), a mini-halo can grow and heat up until atomic line cooling becomes efficient. This scenario can lead to the formation of supermassive ($\gtrsim 10^4\,{\rm M}_\odot$) primordial stars, which may become the seeds of supermassive black holes (Bromm & Loeb 2003; Chon, Hosokawa & Yoshida 2018; Chon & Omukai 2020; Sakurai, Haiman & Inayoshi 2020; Regan 2023; Reinoso et al. 2023; Toyouchi et al. 2023). However, the intrinsically large dynamic range of the problem (which depends on initial conditions for the collapse which are cosmologically rare) complicates forecasting the abundance of such objects. Here, we generate a typical atomic-cooling density–temperature relationship (Fig. 11) using the `collapseUV` test provided with KROME, where the cloud is subject to a Lyman–Werner background $J_{21} = 10^5$, with $J_{21} = J_{\rm LW}/(10^{-21}\,{\rm erg\,s^{-1}\,cm^{-2}\,Hz^{-1}})$.

In this case, we assume an NFW profile for a $10^8\,{\rm M}_\odot$ halo with a concentration parameter $c = 3.3$ (based on the mass concentration relationship of Diemer & Kravtsov 2015), with the normalization calculated by the COLOSSUS package (Diemer 2018). The gas density profile is shown in Fig. 12. We find that (consistent with the nearly isothermal evolution) the gas density scales as the inverse square of

Downloaded from https://academic.oup.com/mnras/article/537/1/580/7943696 by guest on 09 March 2025

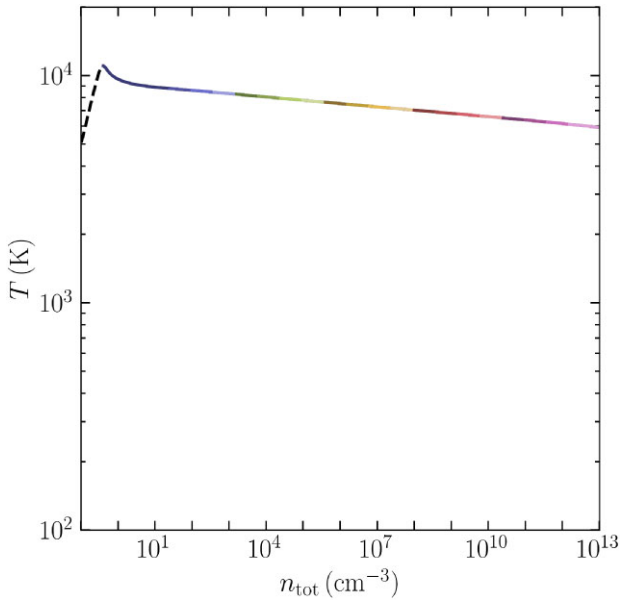

Figure 11. As Fig. 1, but for the atomic-cooling halo. Here, the trajectory is nearly isothermal at the atomic-cooling limit temperature.

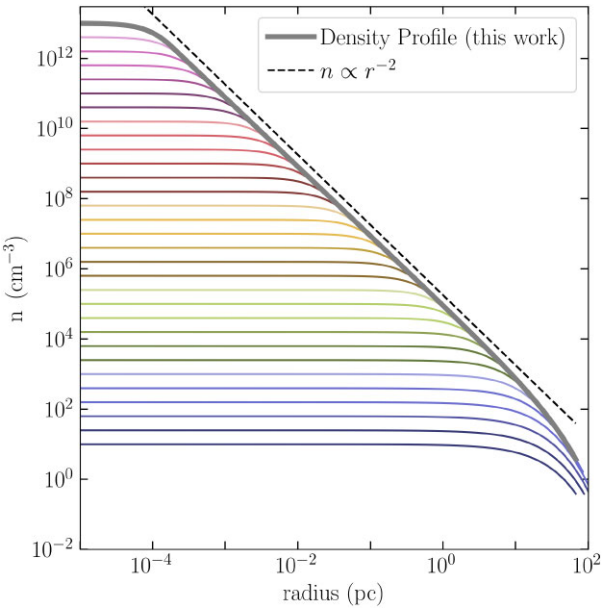

Figure 12. As Fig. 3 but for the atomic-cooling halo. From the nearly isothermal evolution, we expect $n \propto r^{-2}$, which is observed until the dark matter dominates the density at large radii.

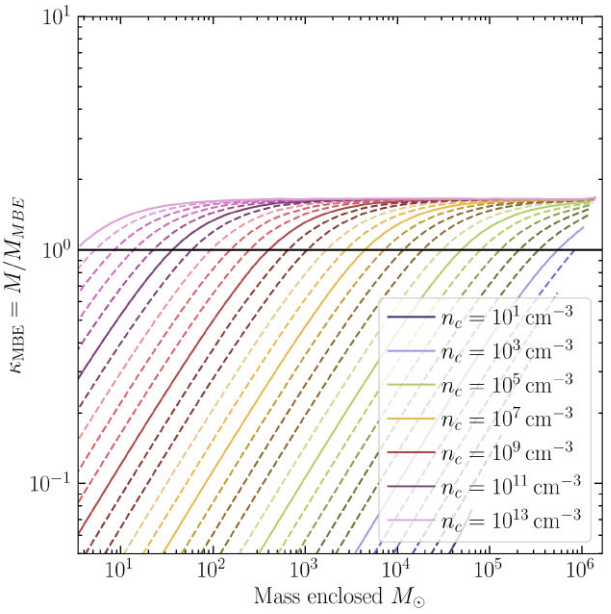

Figure 13. As Fig. 4, but for the atomic-cooling halo. Here, an equal degree of gravitational instability is established out to the initial core mass (i.e. the mass at which $\kappa_{\rm MBE}$ first exceeds unity).

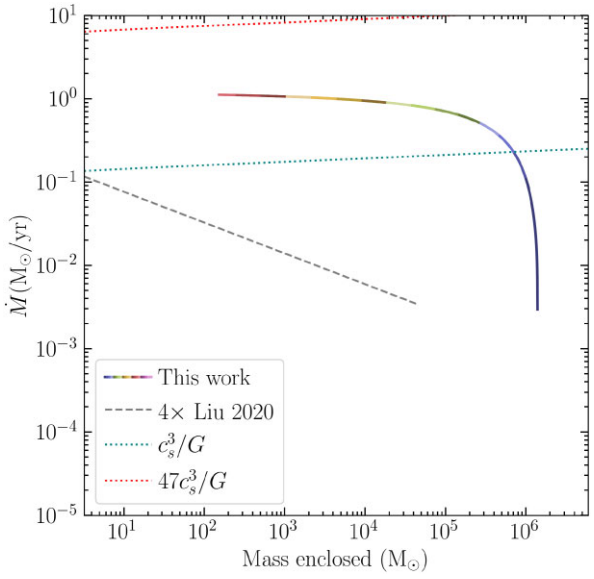

Figure 14. As Fig. 6, but for the atomic-cooling halo. In contrast to the 'shoulder' seen in previous sections (associated with the temperature minimum of the gas), we see an abrupt cutoff in the infall rate beyond the initial core mass.

the radius, until the dark matter becomes important in the calculation of the Bonnor–Ebert radius, around 20 pc. A less concentrated or lower mass dark matter halo would diminish this effect.

We show $\kappa_{\rm MBE}$ in Fig. 13. The nearly isothermal evolution rapidly establishes a dynamical collapse out to the mass scale where the core contraction began (Fig. 14). The characteristic (nearly constant) infall rate $\sim 1\,{\rm M}_\odot\,{\rm yr}^{-1}$ is comparable to that found in the 3D simulations of Latif et al. (2013), which is a case with similar thermal evolution. In the absence of strong features in the density–temperature relationship, the cloud mass is set by the mass where cooling first becomes efficient. This depends on the growth history of the halo, both through the dark matter profile (which helps set the mass enclosed at fixed density early in the collapse) and through the dynamical heating of the gas (which will determine the density at which the gas first reaches the atomic-cooling limit temperature $\sim 10^4$ K). Given such high infall rates, stellar feedback is expected to be suppressed as the protostar will expand significantly to enter a bloating phase under rapid accretion (Omukai & Palla 2001, 2003; Hosokawa et al. 2013; Haemmerlé et al. 2018; Herrington, Whalen & Woods 2023; Nandal et al. 2023). Therefore, combining our infall history with the model in Liu et al. (2024), we predict that a supermassive star of $\hat{M}_\star \sim 6 \times 10^4\,{\rm M}_\odot$ will form in the end, which is expected to collapse directly into a massive black hole seed.

Downloaded from https://academic.oup.com/mnras/article/537/1/580/7943696 by guest on 09 March 2025

4 DISCUSSION

We have developed a model of gravitational collapse regulated by radiative cooling. We have illustrated how the microphysics of the gas control the density and velocity profiles established over the course of the collapse as well as the infall rate. Further, we have presented a newly general and physically precise notion of gravitational instability in this context based on the MBE scale. We have demonstrated the agreement of our results with vastly more sophisticated numerical treatments. Our approach is computationally expedient: generating the full, late time density profile using a grid of 60 central densities takes of the order of a few seconds on consumer hardware, which is dominated by the compile time. With the code pre-compiled and the density–temperature relationship pre-computed, generating the density profile requires only ~ 0.1 s. In certain situations, this speedup compared to hydrodynamical simulations (in exchange for some loss of accuracy) may be useful.

However, our model does not capture the full degree of complexity present in hydrodynamical simulations (let alone reality). For example, Omukai et al. (2010) found in their 1D simulations that strong heating in the core leads to the formation of shocks as the core fails to 'stay ahead' of the infalling material. We have further made no attempt to model phenomena including deviations from spherical symmetry (which can lead to the formation and subsequent fragmentation of an accretion disc), turbulence, magnetic fields, and radiative feedback – all of which are understood to play important roles in the star formation process (e.g. Larson 1973; McKee & Tan 2002, 2003; Tan & McKee 2004; Hennebelle & Chabrier 2008; Hopkins 2012b; Guszejnov & Hopkins 2015; Tsukamoto et al. 2015; Inoue & Yoshida 2020; Kimura, Hosokawa & Sugimura 2021; Liu et al. 2024; Thomasson et al. 2024; Luo et al. 2024b). Some of these shortcomings can be addressed by future work, for example, by the inclusion of additional pressure terms in an effective sound speed.

These caveats do not diminish the utility of our model both as a cross-check for simulations in varying physical environments and as a conceptual framework. We have made precise the sense in which the density–temperature relationship in the core controls the dynamics of the entire collapse, and determines the mass of the eventual collapsing cloud. We clearly distinguish the roles of Rees–Ostriker and Bonnor–Ebert instability criteria in the collapse of thermally supported gas. The distinction is based on the 'two-phase', non-homologous nature of the collapse in which the gas first contracts to protostellar densities and then subsequently falls on to the nascent protostar (or its disc). The Rees–Ostriker criterion controls the onset of runaway contraction in the sense of a gas core rapidly condensing to high density. This phase of the collapse, although it can occur on a dynamical time-scale, is a quasi-equilibrium process.

This runaway cooling in the core is the cause of gravitational instability, rather than the consequence. Then 'dynamical' or Bonnor–Ebert instability impacts the dynamics principally after the formation of the protostar, during the accretion phase. These facts are not widely appreciated. For example, it is common practice to begin cloud-scale simulations of primordial star formation with the density enhanced relative to the hydrostatic value by some constant factor to 'initiate the collapse' (e.g. Omukai et al. 2010; Chon et al. 2021). In fact, in Omukai et al. (2010) by the time of the first snapshot the density profile has 'corrected' to the one calculated in this work (Fig. 3).

Finally, we illustrated that the mass scale at which the core contraction initiates dynamical instability in the envelope depends crucially on the features in the density–temperature relationship: Strong cooling leads to stability and mild cooling or heating leads to instability. With these insights, we can make newly precise statements about the effects of the gas equation of state on the mass scale of the collapse. For example, we have extended the conventional wisdom that a nearly isothermal equation of state (as in our atomic-cooling example) 'suppresses fragmentation' (Li et al. 2003) by showing (Fig. 13) that a nearly isothermal equation of state rapidly establishes gravitational instability at the scale where the core contraction begins, which may lead to a monolithic collapse at this scale. On the other hand, compared to the argument that cooling promotes hierarchical fragmentation down to the temperature minimum, we have shown that strong cooling (as in our delayed collapse example) leads to a nearly hydrostatic envelope, so that a large infall velocity is established only past the temperature minimum. This is true independent of the possible multiplicity of the cores – fragmentation may occur in the envelope, but is not necessary to explain the characteristic mass of collapsing clouds.

By these arguments, we clarify the significance of the 'loitering point' in Population III star formation: the increase in temperature and corresponding steep density profile at densities above the loitering point accelerates the envelope inwards, so that the characteristic mass of the collapsing cloud corresponds to the Bonnor–Ebert mass at this point. We show in Appendix C that the effect of the thermal evolution on the dynamics is exaggerated by the fact that dark matter dominates the potential at densities below the loitering point, further suppressing gravitational instability at low densities.

These ideas differ from pre-existing notions concerning gravitational collapse and fragmentation based on perturbative instabilities in the medium. Because density perturbations grow on the free-fall time-scale, such instabilities are not likely to operate during free-fall core contraction without external forces. Such instabilities become important, for example, when the collapse is delayed (i.e. by inefficient angular momentum transport, resulting in the formation of a disc) or when large density perturbations are established on sub-dynamical time-scales (i.e. by supersonic turbulence). Either or both effect can easily be relevant in realistic situations. Here, we have illustrated the sense in which even a monolithic collapse contains a preferred mass scale dictated by the radiative physics of the gas.

Our model describes the density profile of gas after runaway Kelvin–Helmholtz contraction is initiated. For a fixed density–temperature relationship, the late collapse results are fairly insensitive to the initial conditions. In Sections 3.1 and 3.2, we have developed two representative examples where the cloud/halo scale physics significantly alter the density–temperature relationship, and hence the dynamics of the collapse. In the primordial case considered here, the large-scale initial conditions are dictated by cosmology, and in particular by the distribution of dark matter. In a companion paper (Liu et al. 2024), we develop a model relating the cloud-scale infall rate (as calculated here) with the final stellar mass based on the interplay between radiative feedback and fragmentation, while in Gurian et al. (2024), we predicted the chemical–thermal evolution of the cloud based on the cosmological environment. These efforts can be connected towards a comprehensive analytic model of primordial star formation. This model is able to predict the final mass of stars formed from any input evolution track of primordial star-forming gas in the temperature–density phase diagram with minimal computational cost and physically motivated free parameters (for disc fragmentation, stellar evolution and feedback) rather than phenomenological parameters such as star formation efficiency. It covers all possible modes of Pop III star formation known to date, as illustrated here using the evolution tracks predicted by the one-zone approach for the three examples of H_2- (Section 2), HD- (Section 3.1), and atomic-cooling (Section 3.2) clouds (see also Liu et al. 2024). The universality and flexibility of this model offer

Downloaded from https://academic.oup.com/mnras/article/537/1/580/7943696 by guest on 09 March 2025

promising applications across a wide range of topics. For example, it can be employed to investigate the gravitational, thermal, and chemical impacts of DM physics on Pop III star formation. It can also be incorporated into cosmological simulations and semi-analytical models that account for the large-scale environmental effects (e.g. radiation background of H_2-dissociating photons, dynamical heating by halo mergers, streaming motion between DM and baryons) on (the onset of) Pop III star formation but lack the resolution to fully follow the small-scale cloud collapse and protostar formation/evolution processes. As long as the initial collapse of the cloud at a density scale of $n \sim 10^3 - 10^5$ cm^{-3} is captured in such large-scale models, the final product of subsequent evolution can be easily derived from our analytical model. Exploring such applications is an intriguing direction for future research.

ACKNOWLEDGEMENTS

We thank Kazuyuki Omukai for sharing the data from Omukai et al. (2010) and Kazuyuki Sugimura for sharing the data from Sugimura et al. (2023) . We thank Chris Matzner, Sarah Shandera, and Daisuke Toyouchi for useful discussions. BL gratefully acknowledges the support of the Royal Society University Research Fellowship and the funding from the Deutsche Forschungsgemeinschaft (DFG, German Research Foundation) under Germany's Excellence Strategy EXC 2181/1–390900948 (the Heidelberg STRUCTURES Excellence Cluster). DJ is supported by KIAS Individual grant PG088301 at Korea Institute for Advanced Study. NY acknowledges financial support from JSPS Research grant 20H05847. Research at the Perimeter Institute is supported in part by the Government of Canada through the Department of Innovation, Science and Economic Development Canada and by the Province of Ontario through the Ministry of Colleges and Universities. The development of this work benefited from in-person collaboration supported by the scientific partnership between the Kavli IPMU and Perimeter Institute.

DATA AVAILABILITY

The code and data underlying this paper will be shared on reasonable request to JG at jgurian@perimeterinstitute.ca.

REFERENCES

Bertschinger E., 1989, ApJ, 340, 666
Blumenthal G. R., Faber S. M., Flores R., Primack J. R., 1986, ApJ, 301, 27
Bodenheimer P., Tohline J. E., Black D. C., 1980, ApJ, 242, 209
Bonnor W. B., 1956, MNRAS, 116, 351
Bramante J., Cappiello C. V., Diamond M., Kim J. L., Liu Q., Vincent A. C., 2024a, Phys. Rev. D, 110, 043041
Bramante J., Diamond M., Kim J. L., 2024b, J. Cosmol. Astropart. Phys., 2024, 002
Bromm V., 2013, Rep. Prog. Phys., 76, 112901
Bromm V., Larson R. B., 2004, ARA&A, 42, 79
Bromm V., Loeb A., 2003, ApJ, 596, 34
Bromm V., Coppi P. S., Larson R. B., 1999, ApJ, 527, L5
Chang J. H., Egana-Ugrinovic D., Essig R., Kouvaris C., 2019, J. Cosmol. Astropart. Phys., 2019, 036
Chon S., Omukai K., 2020, MNRAS, 494, 2851
Chon S., Hosokawa T., Yoshida N., 2018, MNRAS, 475, 4104
Chon S., Omukai K., Schneider R., 2021, MNRAS, 508, 4175
Cooke R. J., Pettini M., Steidel C. C., 2018, ApJ, 855, 102
D'Amico G., Panci P., Lupi A., Bovino S., Silk J., 2018, MNRAS, 473, 328
Diemer B., 2018, ApJS, 239, 35
Diemer B., Kravtsov A. V., 2015, ApJ, 799, 108
Ebert R., 1955, Z. Astrophys., 37, 217
Fernandez N., Ghalsasi A., Profumo S., Santos-Olmsted L., Smyth N., 2024, J. Cosmol. Astropart. Phys., 2024, 064
Foster P. N., Chevalier R. A., 1993, ApJ, 416, 303
Freese K., Rindler-Daller T., Spolyar D., Valluri M., 2016, Rep. Prog. Phys., 79, 066902
Grassi T., Bovino S., Schleicher D. R. G., Prieto J., Seifried D., Simoncini E., Gianturco F. A., 2014, MNRAS, 439, 2386
Gurian J., Ryan M., Schon S., Jeong D., Shandera S., 2022, ApJ, 939, L12
Gurian J., Jeong D., Liu B., 2024, ApJ, 963, 33
Guszejnov D., Hopkins P. F., 2015, MNRAS, 450, 4137
Haemmerlé L., Woods T. E., Klessen R. S., Heger A., Whalen D. J., 2018, MNRAS, 474, 2757
Haemmerlé L., Mayer L., Klessen R. S., Hosokawa T., Madau P., Bromm V., 2020, Space Sci. Rev., 216, 48
Hennebelle P., Chabrier G., 2008, ApJ, 684, 395
Herrington N. P., Whalen D. J., Woods T. E., 2023, MNRAS, 521, 463
Hippert M., Setford J., Tan H., Curtin D., Noronha-Hostler J., Yunes N., 2022, Phys. Rev. D, 106, 035025
Hirano S., Hosokawa T., Yoshida N., Umeda H., Omukai K., Chiaki G., Yorke H. W., 2014, ApJ, 781, 60
Hirano S., Hosokawa T., Yoshida N., Omukai K., Yorke H. W., 2015, MNRAS, 448, 568
Hirata C. M., Padmanabhan N., 2006, MNRAS, 372, 1175
Hopkins P. F., 2012a, MNRAS, 423, 2016
Hopkins P. F., 2012b, MNRAS, 423, 2016
Hopkins P. F., 2013, MNRAS, 430, 1653
Hosokawa T., Omukai K., 2009, ApJ, 703, 1810
Hosokawa T., Yorke H. W., Inayoshi K., Omukai K., Yoshida N., 2013, ApJ, 778, 178
Hunter C., 1977, ApJ, 218, 834
Inoue S., Yoshida N., 2020, MNRAS, 491, L24
Inutsuka S.-I., Miyama S. M., 1992, ApJ, 388, 392
Jeans J. H., 1928, Astronomy and Cosmogony. Cambridge Univ. Press, Cambridge
Kimura K., Hosokawa T., Sugimura K., 2021, ApJ, 911, 52
Kiyuna M., Hosokawa T., Chon S., 2023, MNRAS, 523, 1496
Klessen R. S., Glover S. C. O., 2023, ARA&A, 61, 65
Larson R. B., 1969, MNRAS, 145, 271
Larson R. B., 1973, MNRAS, 161, 133
Larson R. B., 1985, MNRAS, 214, 379
Larson R. B., 2005, MNRAS, 359, 211
Latif M. A., Schleicher D. R. G., Schmidt W., Niemeyer J., 2013, MNRAS, 433, 1607
Li Y., Klessen R. S., Mac Low M.-M., 2003, ApJ, 592, 975
Li W., Inayoshi K., Qiu Y., 2021, ApJ, 917, 60
Liu B., Bromm V., 2018, MNRAS, 476, 1826
Liu B., Meynet G., Bromm V., 2021, MNRAS, 501, 643
Liu B., Gurian J., Inayoshi K., Hirano S., Hosokawa T., Bromm V., Yoshida N., 2024, MNRAS, 543, 290
Low C., Lynden-Bell D., 1976, MNRAS, 176, 367
Luo A.-X., Liu H.-L., Li J.-Z., 2024a, preprint (arXiv:2408.16299)
Luo A.-X., Liu H.-L., Li G.-X., Pan S., Yang D.-T., 2024b, Res. Astron. Astrophys., 24, 065003
McKee C. F., Tan J. C., 2002, Nature, 416, 59
McKee C. F., Tan J. C., 2003, ApJ, 585, 850
Matzner C. D., McKee C. F., 2000, ApJ, 545, 364
Nakazato Y., Chiaki G., Yoshida N., Naoz S., Lake W., Chiou Y. S., 2022, ApJ, 927, L12
Nandal D., Regan J. A., Woods T. E., Farrell E., Ekström S., Meynet G., 2023, A&A, 677, A155
Nishijima S., Hirano S., Umeda H., 2024, ApJ, 965, 141
Omukai K., 2001, ApJ, 546, 635
Omukai K., Nishi R., 1998a, ApJ, 508, 141
Omukai K., Nishi R., 1998b, ApJ, 508, 141
Omukai K., Palla F., 2001, ApJ, 561, L55
Omukai K., Palla F., 2003, ApJ, 589, 677

Downloaded from https://academic.oup.com/mnras/article/537/1/580/7943696 by guest on 09 March 2025

Omukai K., Tsuribe T., Schneider R., Ferrara A., 2005, ApJ, 626, 627
Omukai K., Hosokawa T., Yoshida N., 2010, ApJ, 722, 1793
Ostriker J., 1964, ApJ, 140, 1056
Penston M. V., 1969, MNRAS, 144, 425
Qin W., Muñoz J. B., Liu H., Slatyer T. R., 2024, Phys. Rev. D, 109, 103026
Rackauckas C., Nie Q., 2017, J. Open Res. Softw., 5, 15
Rackauckas C. et al., 2020, preprint (arXiv:2001.04385)
Rees M. J., 1976, MNRAS, 176, 483
Rees M. J., Ostriker J. P., 1977, MNRAS, 179, 541
Regan J., 2023, Open J. Astrophys., 6, 12
Reinoso B., Klessen R. S., Schleicher D., Glover S. C. O., Solar P., 2023, MNRAS, 521, 3553
Ripamonti E., Mapelli M., Ferrara A., 2007, MNRAS, 375, 1399
Sakurai Y., Vorobyov E. I., Hosokawa T., Yoshida N., Omukai K., Yorke H. W., 2016, MNRAS, 459, 1137
Sakurai Y., Haiman Z., Inayoshi K., 2020, MNRAS, 499, 5960
Seager S., Sasselov D. D., Scott D., 1999, ApJ, 523, L1
Shandera S., Jeong D., Grasshorn Gebhardt H. S., 2018, Phys. Rev. Lett., 120, 241102
Shu F. H., 1977, ApJ, 214, 488
Sipilä O., Harju J., Juvela M., 2011, A&A, 535, A49
Sipilä O., Harju J., Juvela M., 2015, A&A, 582, A48
Sipilä O., Caselli P., Juvela M., 2017, A&A, 601, A113
Smith B. D., O'Shea B. W., Khochfar S., Turk M. J., Wise J. H., Norman M. L., 2024, MNRAS, 532, 3797
Spolyar D., Freese K., Gondolo P., 2008, Phys. Rev. Lett., 100, 051101
Staff J. E., Tanaka K. E. I., Tan J. C., 2019, ApJ, 882, 123
Sugimura K., Matsumoto T., Hosokawa T., Hirano S., Omukai K., 2023, ApJ, 959, 17
Tan J. C., McKee C. F., 2004, ApJ, 603, 383
Tanaka K. E. I., Tan J. C., Zhang Y., 2017, ApJ, 835, 32
Thomasson B., Joncour I., Moraux E., Motte F., Louvet F., González M., Nony T., 2024, A&A, 689, A133
Tohline J. E., 1980a, ApJ, 235, 866
Tohline J. E., 1980b, ApJ, 239, 417
Toyouchi D., Inayoshi K., Li W., Haiman Z., Kuiper R., 2023, MNRAS, 518, 1601
Tsukamoto Y., Takahashi S. Z., Machida M. N., Inutsuka S., 2015, MNRAS, 446, 1175
White S. D. M., Frenk C. S., 1991, ApJ, 379, 52
Wise J. H., Regan J. A., O'Shea B. W., Norman M. L., Downes T. P., Xu H., 2019, Nature, 566, 85

APPENDIX A: THE COLLAPSE TIME-SCALE

In this work, we take the collapse time-scale $t_{\rm col}$ as a fixed, constant multiple of the freefall time-scale, $t_{\rm col} = f t_{\rm ff}$. Other authors have considered more sophisticated one-zone models. For example, Omukai et al. (2005) adopted the following parameterization to take into account the (temporal) slowdown of the collapse due to the evolution of equation of state:

$$t_{\rm col} = \frac{1}{\sqrt{1-f}} t_{\rm ff}, \tag{A1}$$

where f varies according the ratio of pressure to gravity,

$$f = \begin{cases} 0 & \gamma < 0.83 \\ 0.6 + 2.5(\gamma - 1) - 6.0(\gamma - 1)^2 & 0.83 < \gamma < 1 \\ 1.0 + 0.2(\gamma - 4/3) - 2.9(\gamma - 4/3)^2 & \gamma > 1 \end{cases}, \tag{A2}$$

given $\gamma = \frac{\partial \log P}{\partial \log \rho}$. To implement this in our one-zone model, we avoid unphysical oscillations in f by at each step calculating $\gamma = (\gamma_{\rm old} + \gamma_{\rm new})/2$, where $\gamma_{\rm old}$ is the value adopted at the previous timestep and $\gamma_{\rm new}$ is the value calculated at the current timestep. We show in Fig. A1 that by somewhat reducing the temperature at $n \gtrsim 10^3$ cm^{-3} due to reduced compressional heating, this alternative parameterization has a modest effect on the density profile and hence all the derived quantities in this work. The effect of this parameterization on the other cases is similarly small. However, as the examples in the main text illustrate, a global slowdown in the collapse does significantly alter the chemical–thermal evolution. In Gurian et al. (2024), we studied cases where the global slowdown parameter can be predicted based on the cosmological environment.

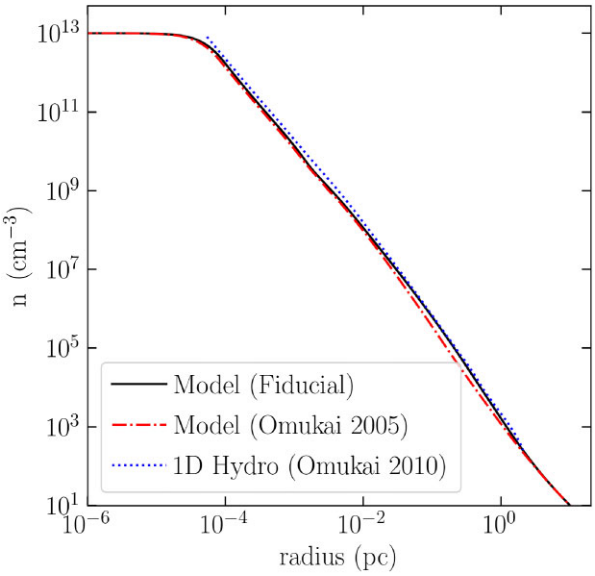

Figure A1. The density profile in the molecular-cooling cloud in our fiducial model (black), our model with the temperature–density relationship calculated as in Omukai et al. (2005) (red, dot–dashed), and in the 1D hydro calculation of Omukai et al. (2010) (blue, dashed).

APPENDIX B: THE BONNOR EBERT MASS

The usual Bonnor–Ebert criterion

$$\frac{\delta P}{\delta V} = 0 \tag{B1}$$

can be written in terms of the change in central density as

$$\left(\frac{\partial P}{\partial \rho_{\rm c}}\right)_M \left(\frac{\partial V}{\partial \rho_{\rm c}}\right)_M^{-1} = 0, \tag{B2}$$

where the subscript M indicates the derivatives are evaluated at fixed mass. The first zero occurs when

$$\left(\frac{\partial P}{\partial \rho_{\rm c}}\right)_M = 0, \tag{B3}$$

because the point of equal mass enclosed (where $\frac{\partial V}{\partial \rho_{\rm c}} = 0$) will occur at larger radius than the point of equal density. This resembles equation (12). Using the chain rule, the Bonnor–Ebert criterion is

$$\left(\frac{\partial P}{\partial \rho_{\rm c}}\right)_M = \left.\frac{\partial P}{\partial \rho}\right|_{\rho=\rho_{\rm HSE}} \left(\frac{\partial \rho_{\rm HSE}}{\partial \rho_{\rm c}} + \frac{\partial \rho_{\rm HSE}}{\partial r}\frac{\partial r}{\partial \rho_{\rm c}}\right) = 0, \tag{B4}$$

where the second term enforces mass conservation via

$$\frac{\partial r}{\partial \rho_{\rm c}} = -\frac{1}{4\pi r^2 \rho}\frac{\partial M}{\partial \rho_{\rm c}}. \tag{B5}$$

We have checked that this formulation equations (B4)–(B5) agrees with equation (3.3) of Bonnor (1956). Clearly, the condition employed in this work equation (13) corresponds to the first term of

Downloaded from https://academic.oup.com/mnras/article/537/1/580/7943696 by guest on 09 March 2025

equation (B4), which corresponds to evaluating the derivative at fixed radius.

APPENDIX C: ROLE OF DARK MATTER

In the H_2 cooling mini-halo, the total density is dominated by dark matter once the gas density drops below $\sim 10^3\,\mathrm{cm}^{-3}$. Both because we do not attempt to self-consistently model the evolution of the dark matter and because the profile adopted equation (10) is highly approximate, we here bracket the effects of our ignorance of the correct profile on our results. In addition to the fiducial profile equation (10), we consider both an NFW profile appropriate to a halo of mass $5 \times 10^5\,\mathrm{M}_\odot$ with a concentration parameter $c = 2.8$ (i.e. a significantly larger dark matter density than the fiducial case) and the case of no dark matter whatsoever. Adiabatic contraction (Blumenthal et al. 1986) of the dark matter in response to the gas collapse can greatly enhance the dark matter density compared to any of these estimates, which may, in turn, have dramatic effects on the star formation process (Spolyar et al. 2008), a possibility we do not treat here. The gas density profiles in our three assumed dark matter profiles are shown in Fig. C1. As we have already argued, the presence of (more) dark matter steepens the density profile.

The accretion rate for all three cases is shown in Fig. C2. In the absence of dark matter, gravitational instability sets in at a lower central density/larger mass scale, because the Bonnor–Ebert (gas) mass at a given central density is larger without dark matter contributing to the potential. A similar phenomenon is observed in simulations of pristine gas clouds separated from dark matter overdensities by supersonic streaming motions, but in that case the density–temperature relationship is additionally modified by the extreme environment (Nakazato et al. 2022).

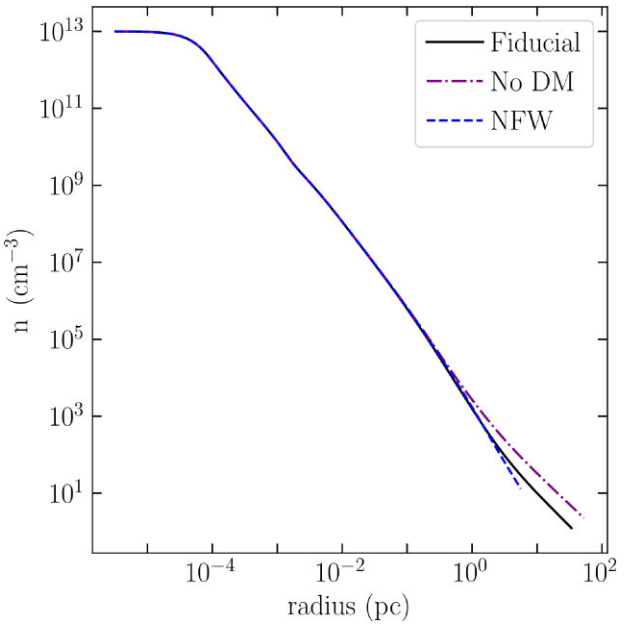

Figure C1. The dependence of the gas density profile in the molecular cooling halo on the assumed dark matter density. The black curve is when the profile is given by equation (10), used in the main text. The purple, dot–dashed curve represents no dark matter, while the blue, dashed curve has an NFW DM profile, for a $5 \times 10^5\,\mathrm{M}_\odot$ halo with a concentration parameter of $c = 2.8$.

APPENDIX D: THE ISOTHERMAL JEANS MASS

In the literature a quantity similar to $\kappa_{\rm BE}$ defined here is often calculated, but instead of the MBE mass defined here, the coefficient is calculated as the isothermal Jeans mass of the mass-weighted temperature and average density:

$$\bar{T} = \tfrac{1}{M}\int_0^M \mathrm{d}M'\,T(M'), \tag{D1}$$

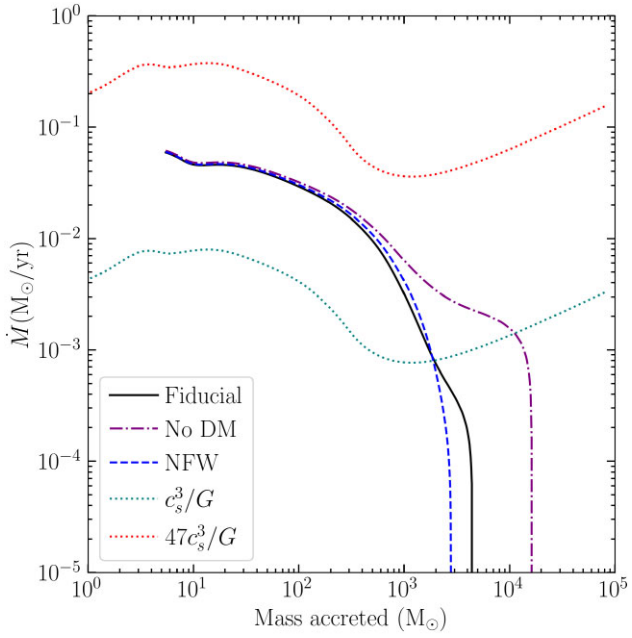

Figure C2. The accretion rate in the molecular cooling halo in the fiducial (black) case, as well as for no dark matter (purple, dot–dashed) and an NFW profile (blue, dashed). The Shu and Larson–Penston values are also shown. With no dark matter, gravitational instability extends past $10^4\,\mathrm{M}_\odot$, albeit at a lower accretion rate.

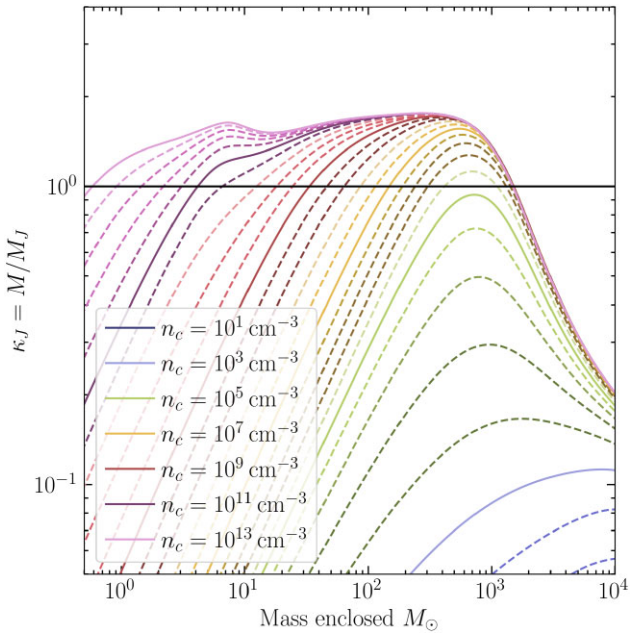

Figure D1. The ratio of the mass enclosed in the molecular cooling halo to the isothermal Jeans mass, computed from the mass-weighted temperature and mean density.

Downloaded from https://academic.oup.com/mnras/article/537/1/580/7943696 by guest on 09 March 2025

$$\bar{\rho} = \frac{3M}{4\pi R^3}, \tag{D2}$$

so that

$$M_{\rm J} \approx 1.44 \left(\frac{k_{\rm B}\bar{T}}{\mu m_{\rm P} G} \right)^{3/2} \bar{\rho}^{-1/2}. \tag{D3}$$

We here calculate κ_J using equation (D3) in our H_2 cooling halo, shown in Fig. D1. The result becomes qualitatively more similar to e.g. fig. 13 of Hirano et al. (2014) and fig. 2 of Smith et al. (2024) in this case. Note that for an isothermal Bonnor–Ebert sphere, equation (D2) will become small outside of the core. This should not, however, be interpreted as indicating a maximum mass scale for gravitational instability.

We point out that $\bar{\rho}$ can also be equated with the one-zone density in Smith et al. (2024). Such a calculation gives a qualitatively correct result without explicating the mechanism by which radiative cooling sources gravitational instability. Compared with Smith et al. (2024), this work does not attempt to model the initial, slow contraction during which the environmental factors establish the chemistry for the runaway collapse. Here, we have demonstrated that (absent non-thermal support) detailed modelling of the evolution of the average density is unnecessary once cooling becomes efficient. As soon as cooling kicks in, $t_{\rm col} \sim t_C$ and the density and mass scale at which gravitational collapse begins are already determined.

APPENDIX E: COMPARISON WITH SIMULATIONS

In the main text, we demonstrated reasonable agreement between the model and the spherically symmetric simulation of Omukai et al. (2010), which adopts the same level of idealization as the model. That comparison showed that the mechanism of gravitational instability identified in this work is plausibly responsible for initiating dynamical gravitational collapse in Pop. III star-forming regions. Now, we compare our model with the 3D hydrodynamical simulations of Hirano et al. (2014), Sugimura et al. (2023), and Nishijima et al. (2024). In the rest of this work, we have adopted density–temperature relationships computed using one-zone models. In fact, the input for the model is a density–temperature relationship, no matter its source. In principle, one could supply the density–temperature relationship from marginally resolved scales in simulations, or by extrapolating simulation results to higher densities using one-zone models. Here, we use the density–temperature relationship from high-resolution simulation results to predict the dynamics in our model and check the extent to which the results agree with the full hydrodynamical result. For reference, we also show the appropriate comparison with the examples considered in the main body of this work. In the H_2 and HD cooling, we have adopted the dark matter profile equation (10), while for the atomic-cooling cases, we adopt the same NFW profile as in Section 3.2. As shown in Appendix C, the qualitative results depend on the presence of dark matter only in the outer region. The purpose of the comparison is two-fold. On one hand, we are testing the importance of 3D effects neglected in the current model. These include small-scale (aspherical) density perturbations, turbulence, and rotation. On the other, we are assessing the accuracy of the one-zone models in determining the thermal evolution, and the effects of any inaccuracies on the dynamics of the collapse. Note, however, that the one-zone models were not specifically tuned to match the simulation cases in terms of initial density, temperature, or (in the HD case) cosmic microwave background temperature.

In Fig. E1, we show the thermal evolution, and associated density profiles and infall rates both in our model (solid) and in hydrodynamics simulations (dashed) for several cases, grouped by the operative cooling mechanism. The thick lines correspond to the examples of Sections 2.1, 3.1, and 3.2, while thin lines correspond to simulations. For H_2 cooling, we consider three cases: two from the cloud-scale simulations of Sugimura et al. (2023) and one from the cosmological zoom-in simulations of Hirano et al. (2014). The two cases from Sugimura et al. (2023) are snapshots when the central density is $\sim 10^{11}\,{\rm cm}^{-3}$ of the high infall rate and low infall rate clouds studied in that work. From Hirano et al. (2014), we consider the average of all clouds with intermediate infall rates (case P2 in that work) when the central density is $\sim 10^{7}\,{\rm cm}^{-3}$. All these clouds have relatively similar thermal evolutions (Fig. E1, top left panel), and the simulated and analytic density profiles from all cases with H_2 cooling agree such that the different cases are difficult to visually distinguish (left middle panel). Note especially the close agreement between the one-zone model and the low infall case of Sugimura et al. (2023), due to their similar thermal evolution. With respect to the infall rates (bottom left panel), the zero-velocity boundary condition in our model is inconsistent with the cosmological infall in Hirano et al. (2014). Moreover, when the thermal evolution is taken from Sugimura et al. (2023) this boundary condition is artificially pushed to high densities/small masses because the thermal evolution is not available at low densities. Still, the model correctly determines $\sim 10^4\,{\rm M}_\odot$ as the scale at which gravitational instability sets in and the large increase in infall rates between 10^3 and $10^4\,{\rm M}_\odot$. The worst agreement is in the strongly rotationally supported, low-infall rate cloud from Sugimura et al. (2023). This is reasonable, since rotation is not explicitly considered in our model (but only partially via the collapse time-scale factor f). The observation that rotational support has a large effect on the infall velocity but a small effect on the density profile has interesting implications for future work.

For HD cooling (middle column of Fig. E1), we consider the average of all clouds with HD cooling from Hirano et al. (2014), when the central density is $\sim 10^{7}\,{\rm cm}^{-3}$. The disagreement in thermal evolution between the simulations and one-zone model propagates to the density profiles and infall rates. Still, the overall agreement and especially the distinction from the H_2 case is reasonable. As in the H_2 case, the underestimate of the temperature at low densities in the one-zone model as compared to these simulations affects the point where $\kappa_{\rm MBE}$ first exceeds unity (Rees–Ostriker criterion), which will only marginally alter the infall rate in the dense, inner region. Unfortunately, the data of Hirano et al. (2014) do not reveal the inner envelope structure at late times due to the low central density. Hirano et al. (2014) also followed the azimuthally symmetrized accretion after protostar formation. While it is not straightforward to directly compare that calculation with our model, we point out that the protostellar accretion rates in that work roughly agree with the predicted infall rate at low masses in our model $\sim 10^{-2}\,{\rm M}_\odot\,{\rm yr}^{-1}$ and that many of the low-mass stars (whose accretion history is less affected by feedback) exhibit the characteristic 'shoulder' in the accretion rate predicted here by the cooling/isothermal evolution in the low-density gas and heating in the high-density gas (fig. 10 in that work).

Finally, turning to the atomic-cooling case (right column), we take a snapshot from the case of Nishijima et al. (2024) where the Lyman–Werner background $J_{21} = 30$, leading to nearly isothermal atomic cooling. In this snapshot, the central density is $\sim 10^{6}\,{\rm cm}^{-3}$. Here, the one-zone and simulation thermal evolution agree very closely except for the initial conditions, and the density profiles are likewise extremely similar. The infall rates again agree to within a factor of few.

Downloaded from https://academic.oup.com/mnras/article/537/1/580/7943696 by guest on 09 March 2025

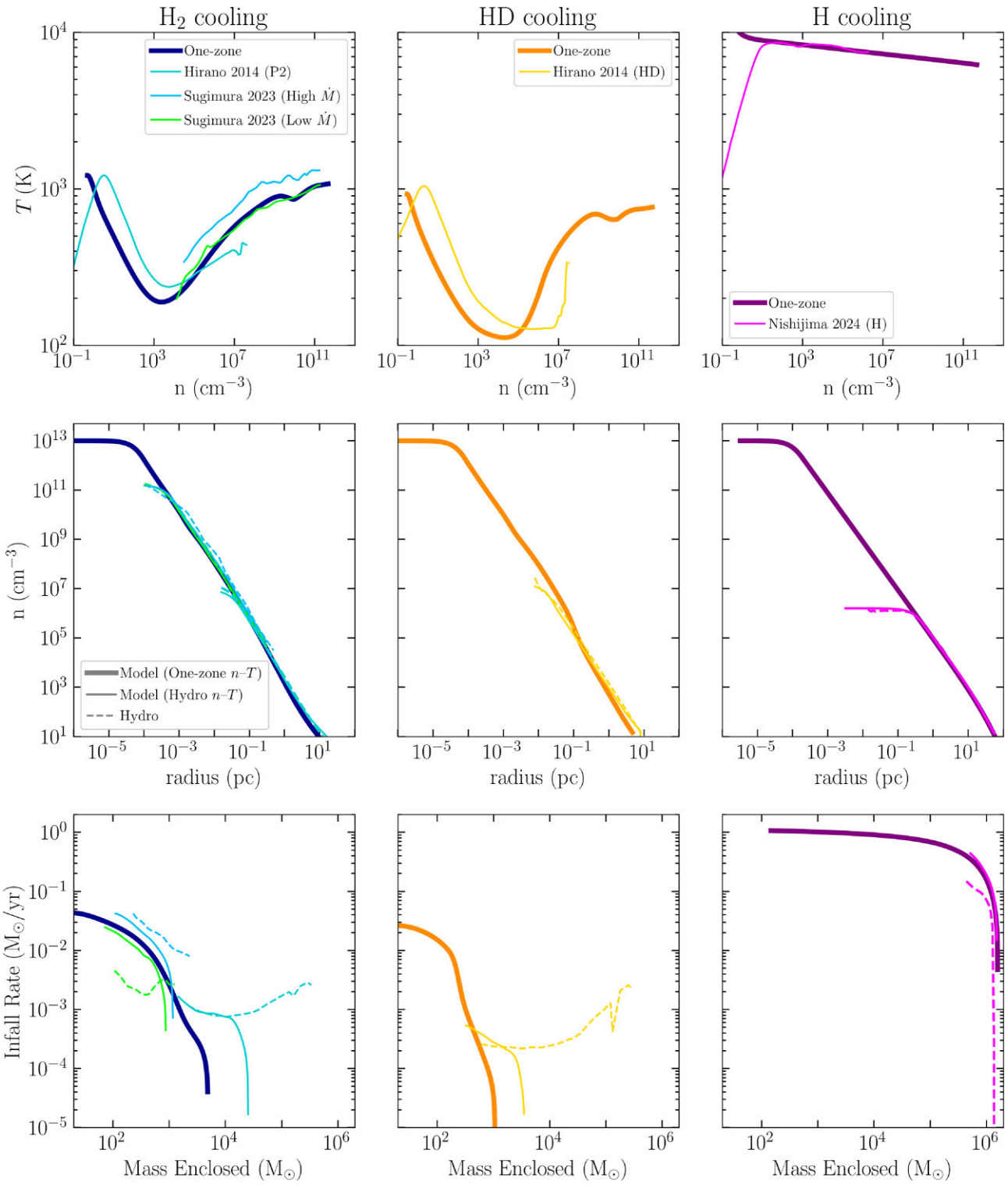

Figure E1. The density–temperature relationships (top row), density profiles (middle row), and infall rates (bottom row) for cases with H_2 cooling (left column), HD cooling (middle column), and H cooling (right column). Thick lines correspond to one-zone density–temperature relationships, while thin lines indicate simulation density–temperature relationships. In the bottom two rows, solid lines indicate predictions of the model, while dashed lines indicate hydro simulation results. Because we do not model the dropoff in velocity near the core, we have truncated the simulation infall rates at $M(r = 25r_{\rm MBE})$, with $r_{\rm MBE}$ determined using our model.

In summary, we find that our model predicts the dynamics of the collapse typically to within a factor of a few using only the thermal evolution, over some four orders of magnitude in cloud mass. The model succeeds at a level comparable to the scatter between individual simulations runs. Moreover, even a crude estimate of the thermal evolution based only on knowledge of the operative cooling mechanism only moderately degrades the accuracy, especially in the

Downloaded from https://academic.oup.com/mnras/article/537/1/580/7943696 by guest on 09 March 2025

dense inner region which is most relevant for star formation. The density profiles especially are determined quite accurately in our model, supporting the notion that the MBE mass defined in this work is indeed a critical scale in the problem. In particular, $\kappa_{\rm MBE}$ is calculated based on the density profile alone and describes the ratio between the actual density profile and the hydrostatic density profile. Thus, the mechanism by which radiative cooling establishes gravitational instability at a characteristic scale, which is a central objective of this work, is robustly demonstrated. The quantitative accuracy of the predictions can be improved both by extending the model to include effects such as rotational and turbulent support and by improving the sophistication with which the chemical-thermal evolution is estimated. These are goals for future work.

This paper has been typeset from a TEX/LATEX file prepared by the author.

Downloaded from https://academic.oup.com/mnras/article/537/1/580/7943696 by guest on 09 March 2025

© 2025 The Author(s).
Published by Oxford University Press on behalf of Royal Astronomical Society. This is an Open Access article distributed under the terms of the Creative Commons Attribution License (https://creativecommons.org/licenses/by/4.0/), which permits unrestricted reuse, distribution, and reproduction in any medium, provided the original work is properly cited.